

**THE ROLE OF TEXTURE EVOLUTION AND STRAIN
HARDENING ON THE ANISOTROPIC RESPONSE
OF POLYCRYSTALLINE METALS**

BY E. ALISAR TUNCER

**A thesis submitted to the
Graduate School—New Brunswick
Rutgers, The State University of New Jersey
in partial fulfillment of the requirements
for the degree of
Master of Science
Graduate Program in Mechanical and Aerospace Engineering**

Written under the direction of

Dr. Alberto M. Cuitiño

and approved by

New Brunswick, New Jersey

October, 2009

ABSTRACT OF THE THESIS

The Role Of Texture Evolution and Strain Hardening on The Anisotropic Response of Polycrystalline Metals

by E. Alisar Tuncer

Thesis Director: Dr. Alberto M. Cuitiño

Anisotropy and texture plays an important role in deformation of Aluminum alloy sheets. The development of anisotropy during metal forming is a key factor as in the standard industrial use of AA – 6022 as stamped automotive body enclosures where a close estimation of anisotropy can deduct costs on both machinery and inventory. In this thesis, we provide a methodology to predict the anisotropic behavior of polycrystalline metals depending on its processing history. The methodology suggested is based on single crystal plasticity model of Cuitiño and Ortiz where the mechanics of dislocation motion through forest dislocations is estimated statistically. In that context, we first study the role of uncertainties and responses of the initial parameters such as initial yield stress and dislocation density. R-values, which is a measure of anisotropy, of a sample undergone hydraulic bulge test are obtained by a uniaxial tensile test simulation and found to be in good agreement with the experimental findings. An optimization method to capture the texture while reducing the number of orientations is introduced and compared with random sets of orientations. Gradual work hardening effect is captured by adjusting the dislocation density carried over through consecutive simulations of rolling and uniaxial stretching. However more accurate models of rolling simulations is necessary to provide r-values and work hardening effect without the need of texture.

Acknowledgements

I am very thankful to all the faculty in the Department of Mechanical and Aerospace Engineering with whom I've had the opportunity to take a class or to discuss a topic. I would also like to thank my M.S. thesis committee members: Prof.George Weng and Prof.Assimina A. Pelegri for spending their valuable time and effort to review, correct and improve this work. I am especially very thankful to my advisor, Prof.Alberto M. Cuitiño for being a huge influence on me with his patience, knowledge, encouragement, and guidance since the very first day I started working with him. I have inherited an exceptional research from him to build my thesis on and without his limitless guidance, this work presented here would not exist. I feel very lucky for being able to continue working with him and for the opportunity to discuss anything, technical or personal. I would also like to thank Dr.Steven Kuchnicki and Dr.Wanjin Chung for their assistance and their prior work which has been a foundation to this thesis.

Thanks to my former graduate director, Prof.Haim Baruh, for his trust and encouragement as well as my current graduate director, Prof.William J. Bottega, for his understanding during my hardest times. I would like to thank every member of Prof.Cuitiño's group, Pedro Romero, Daniel Braido, Srinivas Iyer, and Athanas A. Koynov, for their guidance and their friendship as well as all the graduate students I had the privilege to work with.

Finally, I would like to thank my family, Feride, Sami and Dilan Tuncer, for giving my life a meaning.

Dedication

To my mother, Feride Tuncer
and to my father, Sami Tuncer.

Table of Contents

Abstract	ii
Acknowledgements	iii
Dedication	iv
List of Tables	vii
List of Figures	viii
1. Introduction	1
1.1. Background	2
1.2. Anisotropy and Symmetry	5
1.2.1. Structure	6
1.2.2. Texture	7
1.2.3. Symmetry	7
1.3. R-value and Pole Figures	8
1.4. Review of Relevant Previous Work	10
1.4.1. AA-6022-T43	10
1.4.2. Models	11
1.5. Overview of the Thesis	12
2. Constitutive Framework	15
2.1. Introduction	15
2.2. General Constitutive Framework	15
2.3. Self-Hardening	19
2.4. Cross-Hardening	26
2.5. Summary of the Constitutive Relations	28

3. Sensitivity Analysis	29
3.1. Introduction	29
3.2. Initial Yield Stress	31
3.3. Initial and Saturation Dislocation Density	32
3.4. Self Hardening Parameter	34
3.5. Saturation Shear Strain	35
3.6. Single Slip	36
4. Predicting R-Values	42
4.1. Introduction	42
4.2. Orientation Selection	43
4.3. Numerical Simulation Results	45
4.4. Conclusions	51
5. Effect of Strain Hardening History on R-values	52
5.1. Methodology and Results	53
5.2. Remarks	58
6. Conclusions and Future Work	61
6.1. Summary	61
6.2. Conclusions	62
6.3. Recommendations and Future Work	63
References	2

List of Tables

1.1. Material decomposition of AA-6022 as registered with the Aluminum Association	10
2.1. The $ a $ matrix	27
2.2. Constitutive model parameters for pure aluminum	28
4.1. R-Values	47
4.2. Mean squared errors of selected and randomly chosen orientations . . .	48
4.3. Average Computational time	49
5.1. Constitutive model parameters for pure aluminum in raw stage	55

List of Figures

1.1. Schmid Law	3
1.2. Cup formed by deep-drawing a rolled sheet. The 'ears' are evidence of texture-caused anisotropy. [aluminium.matter.org.uk]	4
1.3. A basic sketch of a layered structure	6
1.4. Forming Pole Figures	9
1.5. Methodology for measuring r-values	10
2.1. Dislocation passing through a randomly distributed point obstacles under monotonic loading	20
2.2. Redistribution of the probability density $f(s, t)$ upon a resolved shear stress increment	23
3.1. Geometric parameters of the hydraulic bulge test	30
3.2. True Stress vs. True Strain with varying initial yield stress	32
3.3. R-values vs. Strain with varying initial yield stress	33
3.4. Active Slip Systems vs. Strain for varying initial dislocation density	34
3.5. Average Dislocation Density vs. Strain with varying initial yield stress	35
3.6. True Stress vs. True Strain with varying initial and saturation dislocation densities (Legend shows the values of initial/saturation densities)	36
3.7. R-values vs. Strain with varying initial and saturation dislocation densities (Legend shows the values of initial/saturation dislocation densities)	36
3.8. Active Slip Systems vs. Strain (Legend shows the values of initial/saturation dislocation densities)	37
3.9. Average Dislocation Density vs. Strain (Legend shows the values of initial/saturation dislocation densities)	37
3.10. Average Dislocation Density vs. Strain for the initial stages of hardening (Legend shows the values of initial/saturation dislocation densities)	38

3.11. True stress strain graph and R - values with varying self hardening parameter	39
3.12. Active Slip Systems and Average Dislocation Density vs. Strain with varying self hardening parameter	39
3.13. True Stress and R-Values vs. Strain with varying self hardening parameter	40
3.14. Active Slip Systems and Dislocation Densities vs. Strain with varying self hardening parameter	40
3.15. Active Slip Systems vs. Strain with varying parameters for the initial hardening stages	41
3.16. Active Slip Systems vs. Strain with varying parameters for the initial hardening stages	41
4.1. {111} Pole figure	45
4.2. {111} Pole figures of selected orientations after hydraulic bulge test. The number of pockets created for 3 Euler angles are shown in parentheses. (↓ RD → TD)	46
4.3. Comparison of R-values	48
4.4. {111} Pole figures showing the texture evolution of 1020 orientations. .	49
4.5. Pole figures of selected orientations after uniaxial elongation.	50
5.1. {111} pole figure after 52% rolling (1020 orientations)	55
5.2. {111} Pole figures showing the effect of history	56
5.3. History effect on true stress with varying history	56
5.4. History effect on average dislocation density with varying history level .	57
5.5. History effect on active slip systems (100 or vs. 1000 or.)	58
5.6. R-values vs Angle	59
5.7. {111} Pole Figure after approximately 50% of uniaxial compression with free lateral expansion	60

Chapter 1

Introduction

Isotropy (from the Greek isos:equal and tropos:rotation) refers to the independence of a feature from the direction. Anisotropy can be defined as the dependence of certain properties on the orientation of the sample with respect to an external frame. In materials science, anisotropy describes the phenomena of chemical bond strengths being directionally dependent. Hence, anisotropy of a property is a result of the arrangement of the *structure* of the material. The concept of anisotropy has been researched extensively, due to the importance of material deformation during many manufacturing processes, mainly rolling and deep-drawing. Being able to estimate the response to a manufacturing process is of great importance, given the costs of manufacturing equipment, fixtures and dies.

The work presented in this thesis contributes to the understanding of the material behavior exhibited by a large grained aluminum alloy sample AA-6022-T43, consequently giving hints on understanding of the response of materials in general. In automobile industry, there is a constant search for better materials to produce more efficient and environment friendly vehicles without sacrificing safety. Currently, cast aluminum components are being used but aluminum alloy sheet materials are about to make their impact as the structural elements for outer and inner body panels. AA-6022-T43 is one of these aluminum alloy sheet products specifically designed to use in automotive industry. Developed and commercialized by Alcoa, AA-6022-T43 series aluminum alloys fulfill the needs of the automotive industry. AA-6022-T43 is easily formable by stamping, which is the most common method to produce enclosure panels, and possesses adequate yield strength to resist dents during service in addition to its resistance to corrosion and good surface finish properties.

This chapter presents an introduction to the field of *texture* and anisotropy as well as a small introduction to AA-6022-T43.

1.1 Background

In crystals, almost all materials of interest are made up from aggregates of single crystals. Single crystals are solid aggregates where the *crystal lattice* is continuous, in other words without grain boundaries. Most commercial metals are composed of aggregates of single crystals, with different atomic orientations with respect to a predetermined external frame, stacked to form polycrystals with grain boundaries. Polycrystals are collection of different orientations of the atomic structure. Deformation processes in polycrystalline metals are always accompanied by a change of crystallographic orientation of each grain, which is often referred as *texture evolution*. The control of the texture evolution in metal-forming processes is of significant interest in modern industry for the purpose of specific anisotropic mechanical properties in the final products. With the advance of computational materials science in recent years, modeling and simulation has provided powerful tools both for theoretical investigations and industrial applications of texture evolution in polycrystalline metals [29].

Predicting the anisotropy of polycrystals involves modeling of single crystals and execution of a physically correct averaging technique for combining single crystal properties into polycrystal behavior. Plastic yielding of single crystals generally occurs by shearing on selected crystallographic slip systems according to Schmid Law. Experiments showed that slip occurs when the shear stress acting in the slip direction on the slip plane reaches some critical value. This critical shear stress is related to the stress required to move dislocations across the slip plane. Consider applying a tensile stress along the long axis of a cylindrical single crystal sample with cross-sectional area A , as shown in figure 1.1.

The applied force along the tensile axis can be defined as $F = \sigma A$. If slip occurs on the slip plane shown in the diagram, with plane normal \mathbf{n} , then the slip direction will lie in this plane as shown in the figure. We can calculate the resolved shear stress acting parallel to the slip direction on the slip plane as follows. The area of the slip plane is

$A/\cos(\phi)$, where ϕ is the angle between the tensile axis and the slip plane normal. The

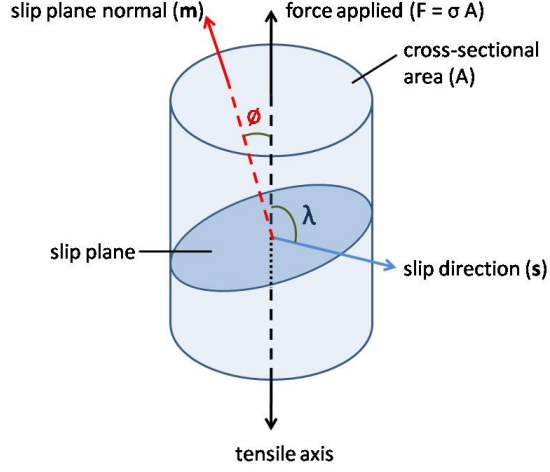


Figure 1.1: Schmid Law

component of the axial force, F , that lies parallel to the slip direction is $F \cos \lambda$. The resolved shear stress on the slip plane parallel to the slip direction is therefore given by:

$$\tau_R = \frac{\text{resolved force acting on the slip plane}}{\text{area of the slip plane}} = \frac{F \cos \lambda}{A / \cos \phi} = \sigma \cos \lambda \cos \phi \quad (1.1)$$

Schmid Law states that the *resolved shear stress*, τ_R , is constant in a given material with specified dislocation density and purity. This resolved shear stress is called *critical shear stress*, τ_C and used as an important parameter to define the deformation of materials. As a result of this mechanism, the plastic flow comes along with an anisotropy of stress and strain components and with lattice rotations that cause orientation changes.

The orientation distribution in a polycrystal is the result of the manufacturing process and thus texture contains detailed information about the history of the piece. Texture has huge influence on properties that it contains information on the relation between parameters of processes and performance of material. For instance, in many materials, during solidification from the melt the crystallites grow in a way that the lattice direction is aligned with the direction of the heat flow. Even this information is good enough to realize the heat flow direction by only looking at the texture orientation.

Conversely, the preferred texture orientation can be obtained by changing the heat flow direction as well as other solidification conditions and manufacturing techniques. These preferred texture orientations may lead to tougher, more resistive or easily deformable products.

The combined effect of deformation and recrystallization is not easily treated theoretically and offers a wide variety of possibilities but for metallurgical applications huge amount of empirical data has been collected and using these knowledge, standardized treatment procedures has been prepared.

During the manufacturing process of face-centered cubic (fcc) wires the deformation causes the $\langle 111 \rangle$ crystal directions to align with the drawing direction. Primary recrystallization relaxes this texture into a $\langle 100 \rangle$ fiber. Applying suitable combination of drawing and annealing the distribution can be varied between these two fibers. In gold wires, $\langle 111 \rangle$ fiber produces higher tensile strength. By carefully controlling the drawing and annealing processes two samples from same batch can accommodate different rupture stresses.



Figure 1.2: Cup formed by deep-drawing a rolled sheet. The 'ears' are evidence of texture-caused anisotropy. [aluminium.matter.org.uk]

For more complex processes, crystallographic texture also has a remarkable effect on the performance of commercial products. One of the most significant example is earing of sheet materials [figure 1.2]. These steel and aluminum sheet products are widely used in automotive industry. Sheet products are stamped and stretched to form the panels of the body. Texture analysis provides the necessary feedback to better the results of the manufacturing by adjusting the thermo-mechanical history of the

material.

Some ferromagnetic materials are also a target of great interest due to their commercial and technological uses. For instance, in iron-silicon alloys with the cube texture, magnetic saturation is achieved by aligning the $\langle 001 \rangle$ -directions with the preferred direction of the magnetic field.

Another peculiar area of texture research is earth sciences. The aim of geology is to analyze the thermo-mechanical history of the Earth. As in material sciences, lattice rotations along specific positions are characteristic of a certain deformation directions. Thus, the analysis of the texture evolution during deformation can be used to determine the slip properties of the process and, conversely, the deformation history can also be deduced from the texture analysis.

Texture and anisotropy is a traditional field of materials science which has seen progress during the past few decades including the interdisciplinary studies. The research conducted on the subject made it possible to determine the texture rapidly in widely available laboratories. Moreover, physical models are developing rapidly to capture the evolution obtained in laboratory test. These results can be represented with methods perfected during the research progress and these measured texture data can be used to quantitatively predict the anisotropic material behavior by computational models. Clearly, texture evolution and application plays its part in many important scenarios for the interrelation between microstructure and properties for process control and material performance.

1.2 Anisotropy and Symmetry

A material being anisotropic or isotropic depends on the composition of the building blocks which we call *structure*. The structural elements responsible for anisotropy are the shape and the *orientation* of the grains rather than their size. The aggregate of crystallite orientations is called the *texture*. The anisotropy of a property is generally affected by *symmetry* considerations. In the following sections, I will try to clarify these terms.

1.2.1 Structure

It is assumed that all the properties of a material sample can be defined by totality of its structural elements such as crystal arrangement, defects structure. *Property* of a material is the relation between a macroscopic action and a macroscopic reaction. The relationship is provided by material property or constitutive relation.

If we look at the crystal structure in figure 1.3, it would be expected that the properties in the layer may be different from properties in the y-direction. If a unit temperature gradient is applied, the heat flow would be expected in a different direction. The property which defines the direction and intensity of the heat flow is 'thermal conductivity' in this case.

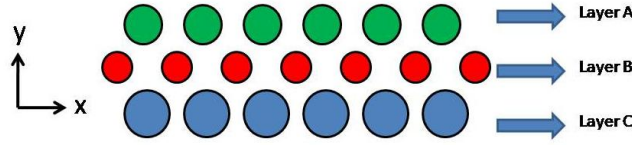


Figure 1.3: A basic sketch of a layered structure

When generalized the macroscopic response, \mathbf{r} , to the given macroscopic stimulus, \mathbf{s} , is related by a material property, κ and shown as:

$$\mathbf{r} = \kappa \cdot \mathbf{s} \quad (1.2)$$

These variables are tensorial characters and the rank of the material property tensor depends on the rank of the stimulus and the response. A tensor of a rank that is equal to the sum of the ranks of the variables is required to satisfy the linear relation. In a common case where the variables \mathbf{r} and \mathbf{s} are vectors (a tensor of a rank one) then the material property is a second rank tensor. By definition, the diagonal coefficients of κ need not to be equal to satisfy the condition necessary for anisotropy. The basic structural element for most materials is the crystal structure and if the structure can be idealized into having translation symmetry then the material is called *crystalline*. The locally grouped atoms form a pattern and these patterns are repeated throughout the

material, on a *lattice*. Even if any real material has some lattice defects, the symmetry properties of crystals are determined by the symmetry of the lattice. Further, a lattice can be characterized by a *unit cell*. The simplest unit cell is a *cube*. It has a high symmetry due to equal lengths and right angles it is characterized by. If one of the axis lengths is different from the other, it is called *tetragonal*. If all axis lengths are different, one obtains the *orthorhombic* lattice.

1.2.2 Texture

The composure of the grains with crystal structures of different orientations may tend to behave differently for different manufacturing operations. For instance, a sample undergoing a rolling operation may have some crystal axes aligned along the rolling direction and forms a particular texture. The same sample subjected to another manufacturing technique can respond with crystal alignment completely different and may form a completely different texture. Depending on the manufacturing process, materials show typical orientation maps which are called preferred orientations. The ability to simulate these textures can be very beneficial to predict the macroscopic response of the sample. Another challenge is to visualize these preferred textures. Standard x-ray diffraction techniques are used to visualize the texture of an experiment sample. In this thesis, to identify and compare the textures generated during the simulations, pole figures are often used. Anisotropy is observed by a parameter called R-value which is defined as the ratio of the width-strain to the thickness-strain. Pole figures and R-values are explained in the section 1.3.

1.2.3 Symmetry

There may be symmetry in the material or simply the property under observation may have symmetrical properties. To explain symmetry in a way that it is appropriate for the rest of the thesis, let us assume a rotation operator, \mathbf{R}

$$\mathbf{R} = \begin{pmatrix} \cos \theta & \sin \theta & 0 \\ -\sin \theta & \cos \theta & 0 \\ 0 & 0 & 1 \end{pmatrix} \quad (1.3)$$

which performs a counter-clockwise rotation around the z-axis by an angle of θ . By this rotation the initial coordinate system, \mathbf{T} , becomes \mathbf{T}'

$$\mathbf{T}' = \mathbf{R} \cdot \mathbf{T} \cdot \mathbf{R}^T \quad (1.4)$$

For some particular forms of \mathbf{R} , \mathbf{T} must be equal to \mathbf{T}' which shows how the symmetry would affect the tensor property \mathbf{T} . The anisotropy of a property is defined by two ingredients: the anisotropy of the particular property in single crystals of the material and the absence of symmetry in the sample. The most important symmetry element a property may have is *centrosymmetry* or in other words a 'center of inversion'. The inversion operator is:

$$\bar{\mathbf{I}} = \begin{pmatrix} -1 & 0 & 0 \\ 0 & -1 & 0 \\ 0 & 0 & -1 \end{pmatrix} \quad (1.5)$$

which means that the quantity which relates the response to the stimulus remains the same when the signs of all coordinates of the stimulus and the response are changed. One other symmetry operator is 'a mirror plane'. For the third axis, it can be expressed as:

$$\mathbf{M} = \begin{pmatrix} 1 & 0 & 0 \\ 0 & 1 & 0 \\ 0 & 0 & -1 \end{pmatrix} \quad (1.6)$$

In mirror symmetry the axis in consideration changes sign, everything else stays unchanged. There are 32 possible combinations of rotations, mirror planes and inversion center, called the *crystal classes* in texture analysis.

1.3 R-value and Pole Figures

Pole figures are standardized projection graphs for the whole set of single crystals in a polycrystal. First, depending on the single crystal structure, a pole is assigned to the crystal structure. During deformation, the orientation of the crystal structure in the grains would change and consequently the direction of the pole. If we think of the grain and the texture within as a brick, the pole would correspond to one of the

orthogonal axes of the brick or multiple poles are assigned, for instance 4 poles for $\{111\}$ pole figure. Figure 1.4 shows an imaginary sphere drawn around the brick. If the "south" pole of the sphere and the intersection of the pole and the sphere is connected by a line exceeding further to the projection plane, pole figure for the certain texture can be obtained. Figure 1.4 depicts two possible orientations and their projections on the pole figure graph. Certain manufacturing processes of different materials have their unique texture evolution which can be observed by pole figures created and the material responses can be estimated by analyzing these pole figures.

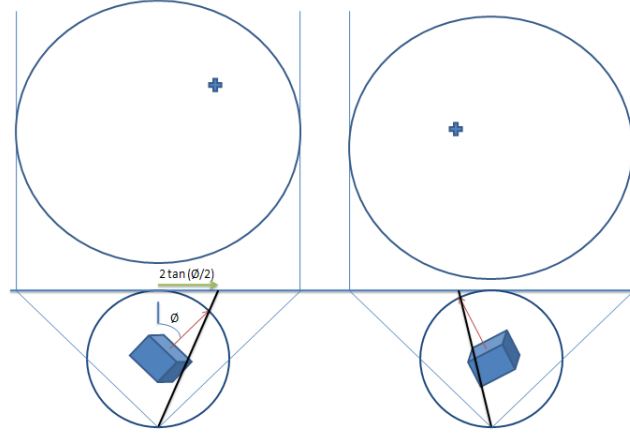


Figure 1.4: Forming Pole Figures

R-value is a measure of anisotropy in terms of the ratio of transverse plastic strains. It is generally measured after the specimen has failed or after a certain strain. In the experimental data provided for this thesis, the r-values are measured after 28% plastic strain. Figure 1.5(a) explains how r-values are measured. R-Values are commonly measured after rolling operations. After rolling, samples are taken from the sheet material for different angles and tensile test is conducted to obtain plastic strain in every direction. In this thesis, the angles are chosen between $0^\circ - 90^\circ$ for every 15° . Figure 1.5(b) shows how the samples are taken from the sheet material to obtain r-values for different angles. An r-value being in the vicinity of 1 means that the investigated property shows isotropy for the chosen direction.

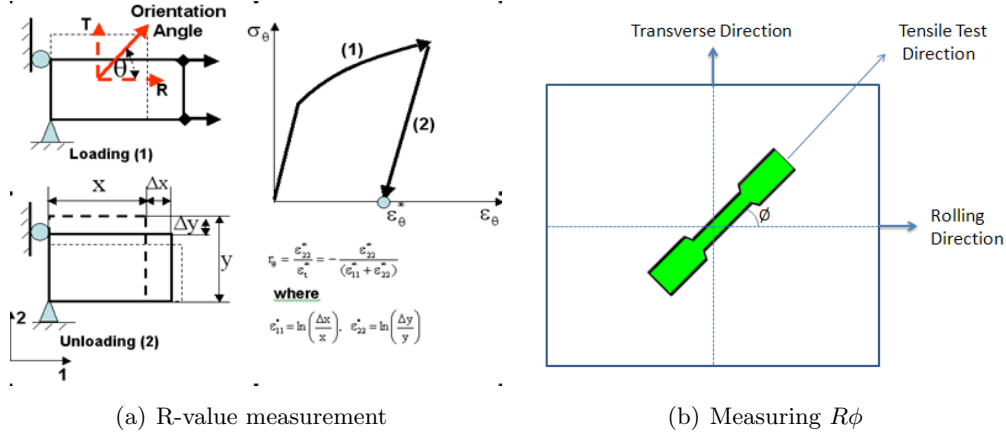


Figure 1.5: Methodology for measuring r-values

1.4 Review of Relevant Previous Work

1.4.1 AA-6022-T43

Alcoa developed aluminum alloy sheet 6022 for the automotive industry in the late 1980's with original thermal treatment code of -T4E29. It has been registered with the Aluminum Association as -T43 when commercialized and it is in the class of Al-Mg-Si alloys. Aluminums in 6000 series utilize magnesium and silicon in various proportions to form magnesium silicide, which makes them heat treatable. Magnesium silicide alloys possess good formability and corrosion resistance with high yield strength in general. AA-6022 material composition can be seen in table 1.1. Manganese and chromium additives increase the strength, mainly by controlling the grain size. Copper ingredient increases the strength in return of corrosion resistance.

Table 1.1: Material decomposition of AA-6022 as registered with the Aluminum Association

Si	Fe	Cu	Mn	Mg	Cr	Zn	Ti	Others (Total)
.8 – 1.5	.05 – .2	.01 – .11	.02 – .10	.45 – .7	.1	.25	.15	.15

AA-6022 is a new alloy with little data in the literature. There has been some research conducted on mechanical and microstructural properties. Wang and Kassner [56] has performed tensile and fatigue tests to summarize the general behavior of AA-6022 as resilient to fatigue, ductile with moderate tensile strength. Miao and Laughlin

have conducted experiments to observe the precipitation and aging mechanisms [38] and effects of Cu content and preaging on precipitation [39]. Observations on precipitate evolution were documented by Brabie and Sridhar [7]. Recently, generalized necking criterion ([11]) and weldability of AA-6022 among other commonly used aluminum alloys ([41]) have also been researched.

1.4.2 Models

The theories on monocrystalline plasticity dates back to the early 20th century and experiences involvement of many investigators, including: Taylor and Elam [51] on distortion of an aluminum crystal which initiated with the idea that there exists presumed slip planes, on which slipping takes place. Schmid [50] presented experimentally that a crystal slip would occur on a given system when the shear stress resolved on the glide reaches a critical value. Taylor's [52] work was the pioneering theory between single and poly crystals which is still being used due to its simplicity. Sachs' [48] theorem was similar to Taylor's model but by contrast, Sachs assumed only one slip system with the highest resolved shear stress can be activated due to the externally imposed stress. Bishop-Hill model [6] followed Taylor's basic assumption to create the classical Taylor-Hill-Bishop model in which intracrystalline deformation in terms of slip along discreet slip systems is described and all the individual grains in the polycrystal are assumed to experience the same deformation gradient history. As the crystal slips along a slip system, the crystallographic lattice reorients into alignment with respect to the flow field to develop a lattice preferred orientation microstructure. In Taylor's model, the slip systems to accommodate the strain is determined by minimizing the net internal work. Taylor-Hill-Bishop model uses the principle of maximum work to compute single crystal and polycrystal yield surfaces. Asaro and Needleman [1] introduced rate dependence into the Taylor model.

This thesis strictly follows the model of Cuitiño and Ortiz [12]. This model shows that, for monotonic loading, the kinetic equation governing the motion of a dislocation line through a random array of point obstacles can be solved in closed form and the solution includes the case in which the density of point obstacles is a

function of time. Franciosi *et al.* [19], Franciosi [15], [16], [17], [18] and Franciosi and Zaoui [20] introduced that the strength of the short-range obstacles introduced by forest dislocations are a function of the mode of interaction. Latent hardening ratios (LHR) are investigated and compared with experiments for aluminum and copper [19]. Closed set of constitutive relations are obtained by building on the work of Gillis and Gilman [21] and Essmann and Rapp [14] by formulating the equations of evolution in terms of dislocation densities. Dislocation density is formulated as a function of slip activity as in equation 5.3.

Recent work on dislocation-based model shows differences between model of Bassani and Wu ([57], [4], [3]) and Pierce *et al.* [44] in terms of latent-hardening effects by means of the hardening matrix. The former proposed a model where the hardening matrix is diagonally dominant and the latter with the hardening matrix in which the off-diagonal terms are dominant. The base model [12] used in this thesis relies on the understanding that these two models are complementary by defining two characteristic resolved shear stresses: yield stress and a characteristic stress obtained by back-extrapolation of the stress-strain curve which is roughly coincident with the flow stress, former related to slip increments by a diagonal hardening matrix and latter are driven by an off-diagonally dominant hardening matrix. The latter procedure is adopted for the interpretation of latent hardening experiments ([28], [46]). The recent work of Cuitiño and Ortiz notes that this difference stems largely from the definition of flow stress adopted. The dislocation-based model used for this thesis conforms to the general structure suggested by Bassani and Wu and the hardening matrix, $h^{\alpha\beta}$, entering the hardening relations is predicted to be diagonal.

1.5 Overview of the Thesis

The work presented in this thesis is organized in the following order:

1. *Chapter 1:* Background and Major Relevant Studies
2. *Chapter 2:* Formulation of General Constitutive Framework
3. *Chapter 3:* Sensitivity Analysis of Aluminum Alloy 6022-T43 with experimental

data

4. *Chapter 4:* Prediction of Anisotropy Parameters with Experimental Data and Optimization of the Model
5. *Chapter 5:* Analysis of the Effect of Dislocation History
6. *Chapter 6:* Summary, Conclusions and Future Work

The thesis begins with *chapter 1* with the general introduction to the field of dislocation based modeling with an emphasis on models which has been the basis of this research. Summary of the majority of pioneering scientific studies performed over the last several decades is provided.

In *chapter 2*, the thesis presents the description and formulation of single crystal dislocation model with statistical approach. Some background on the general form of the constitutive relations for ductile crystals as well as hardening relations are discussed. The theories considered are mainly the motion of a dislocation segment through forest dislocations, the short-range interactions between pair of dislocations and the strength of the resulting intersections as they are treated as obstacles for the dislocation segments, and the kinetics of dislocation multiplication. The kinetic equation governing the motion of a dislocation line through a random distribution of point obstacles is introduced to be solved in closed form where the density of the point obstacles is a function of time.

In *chapter 3*, the experimental texture supplied by the Alcoa laboratories will be used to analyze the responses to by tweaking certain parameters. The changes in hardening and the anisotropy of the material due to the parameter (initial yield stress, initial and saturation dislocation density, self hardening parameter and saturation shear strain) variations will be investigated as well as the evolution of dislocation density and active slip systems. The initial stages of hardening will be presented to observe possible single slip traits in the last section of chapter 3.

In *chapter 4*, the prediction of r-values, texture evolution and the performance of the model will be the main objectives. The r-values and the texture evolution in form of pole figures will be obtained and compared to the experimental results. For

performance studies the notion of speed of the numerical scheme depending linearly on the number of orientations in the texture will be used to optimize the computation time. An orientation selection method depending on the distribution of the orientations will be introduced. The performance of these selected orientations will be compared to the total number of orientations and randomly selected orientations to prove the applicability of this method, focus being on r-values and texture evolution.

Chapter 5 is devoted to the analysis of work hardening effect on the material after rolling. On the contrary to the previous chapters, the simulation of the rolling process will also be conducted to obtain history in terms of dislocation density remained in the polycrystal aggregate. After rolling simulation, the further simulations will be conducted ‘with history’ and ‘without history’. Work hardening will be carried as strain in slip systems due to dislocation density being a function of strain.

Finally, in *chapter 6*, the thesis presents a brief summary along with a set of concluding remarks for the work presented. The work that could be undertaken in the near future to extend the applicability of the formulated theories and the limitations to the model will be noted.

Chapter 2

Constitutive Framework

2.1 Introduction

The current model of Cuitiño and Ortiz [12] is based on the assumption that the total deformation of a crystal is the result of two main mechanisms: dislocation motion contained within the active slip system and lattice distortion. The kinetic equations governing dislocation motion are solved in closed form for monotonic loading, with changes in the dislocation density accounted for. This solution is then completed with suitable equations of dislocation evolution to provide a complete description of the hardening of crystals. The theories considered in this chapter are: The motion of a dislocation line through obstacles formed by forest dislocations, the interactions between pair of dislocations and strength of the resulting intersections, the kinetics of dislocation multiplication. The motion of dislocations through point obstacles formed by forest dislocations based on the statistical mechanical theory proposed by Ortiz and Popov [42]. Firstly, for completeness of the thesis we present the theory behind the computational model of Cuitiño and Ortiz. For more detailed information, reader should refer to *Computational Modelling of Single Crystals*[12].

$$\int_{B_0} \mathbf{P}_{n+1} : \nabla_0 \eta \mathbf{dV}_0 - \int_{B_0} \mathbf{f}_{n+1} \cdot \eta \mathbf{dV}_0 - \int_{\partial B_0} \mathbf{t}_{n+1} \cdot \eta \mathbf{dS}_0 = 0 \quad (2.1)$$

2.2 General Constitutive Framework

Deformation gradient, \mathbf{F} , accounts for both dislocation motion and lattice distortion. Deformation gradient \mathbf{F} can be decomposed into two parts:

$$\mathbf{F} = \mathbf{F}^e \mathbf{F}^p \quad (2.2)$$

where \mathbf{F}^p is the plastic deformation gradient contains the deformation due to dislocation motion and \mathbf{F}^e is the elastic deformation gradient which accounts for the lattice distortion and rotation. As Teodosiu [53] and others [2, 35, 23, 24, 47] suggested, \mathbf{F}^p can be assumed volume-conserving and to leave the crystal lattice undistorted and unrotated. Lattice distortion and rotation are presumed to be contained in the elastic deformation gradient. Thus the deformation power per unit undeformed volume takes the form

$$\mathbf{P} : \dot{\mathbf{F}} = \bar{\mathbf{P}} : \dot{\mathbf{F}}^e + \bar{\boldsymbol{\Sigma}} : \bar{\mathbf{L}}^p \quad (2.3)$$

where $\bar{\mathbf{P}}$ defines the first Piola-Kirchhoff stress tensor relative to the intermediate configuration $\bar{\mathfrak{B}}_t$, given by

$$\bar{\mathbf{P}} = \mathbf{P} \mathbf{F}^{pT} \quad \bar{\boldsymbol{\Sigma}} = \mathbf{F}^{eT} \mathbf{P} \mathbf{F}^{pT} \quad \bar{\mathbf{L}}^p = \dot{\mathbf{F}}^p \mathbf{F}^{p-1} \quad (2.4)$$

and $\bar{\boldsymbol{\Sigma}}$ is a stress measure conjugate to the plastic velocity gradients on the $\bar{\mathfrak{B}}_t$ which is defined as

$$\bar{\mathbf{L}}^p = \dot{\mathbf{F}}^p \mathbf{F}^{p-1} \quad (2.5)$$

The work conjugacy relations (2.3) suggest forms for plastic flow rules and elastic stress-strain relations of the general form

$$\bar{\mathbf{L}}^p = \bar{\mathbf{L}}^p(\bar{\boldsymbol{\Sigma}}, \bar{\mathbf{Q}}) \quad (2.6)$$

$$\bar{\mathbf{P}} = \bar{\mathbf{P}}(\mathbf{F}^e, \bar{\mathbf{Q}}) \quad (2.7)$$

where $\bar{\mathbf{Q}}$ denotes some appropriate set of internal variables defined on $\bar{\mathfrak{B}}_t$, for which the evolution equations are to be supplied. The most general form of (2.7) consistent with the principle of material indifference is

$$\bar{\mathbf{P}} = \mathbf{F}^e \bar{\mathbf{S}}(\bar{\mathbf{C}}^e) \quad (2.8)$$

where $\bar{\mathbf{C}}^e$ is the elastic right Cauchy-Green deformation tensor defined by

$$\bar{\mathbf{C}}^e = \mathbf{F}^{eT} \mathbf{F}^e \quad (2.9)$$

$\bar{\mathbf{S}} = \bar{\mathbf{C}}^{e-1} \bar{\boldsymbol{\Sigma}}$ is a symmetric second Piola-Kirchhoff stress tensor relative to the intermediate configuration $\bar{\mathfrak{B}}_t$. For metals, a linear relation between $\bar{\mathbf{S}}$ and the elastic

Lagrangian strain, $\bar{\mathbf{E}}^e = (\bar{\mathbf{C}}^e - \mathbf{I})/2$, can be assumed without loss of generality. Higher order moduli are available by Teodosiu[54].

From the kinematics of dislocation motion, Taylor [52] and Rice [47] has shown that the formulation of $\bar{\mathbf{L}}^p$ used here has the form

$$\bar{\mathbf{L}}^p = \sum_{\alpha} \dot{\gamma}^{\alpha} \bar{\mathbf{s}}^{\alpha} \otimes \bar{\mathbf{m}}^{\alpha} \quad (2.10)$$

where $\dot{\gamma}^{\alpha}$ is the shear rate on slip system α , for which \mathbf{s}^{α} and \mathbf{m}^{α} are the slip direction and slip plane normal, respectively. The usual assumption which is an extension of Schmid's law states that these slip rates depend on stress through the corresponding resolved shear stress τ^{α} only, i.e.

$$\dot{\gamma}^{\alpha} = \dot{\gamma}^{\alpha}(\tau^{\alpha}, \bar{\mathbf{Q}}) \quad (2.11)$$

If 2.11 is assumed to hold, then it was shown by Rice [47] and by Mandel [35] that the flow rule 2.10 derives from a viscoplastic potential. For completeness $\bar{\mathbf{Q}}$ in the above equation need to be provided. Peirce et al. [43] and several others have proposed a representation for the slip rates,

$$\dot{\gamma}^{\alpha} = \begin{cases} \dot{\gamma}_0^{\alpha} \left(\frac{\tau^{\alpha}}{g^{\alpha}} \right)^{\frac{1}{m}} & \tau^{\alpha} \geq 0 \\ 0 & \text{otherwise} \end{cases} \quad (2.12)$$

where m is a strain-rate sensitivity exponent, $\dot{\gamma}_0^{\alpha}$ is a reference strain rate, and g^{α} is the current flow stress on the slip system α . Cuitiño and Ortiz [12] presented another form of this law to overcome the unrealistic slip strain rates noted by several authors [32, 34, 37], for values of τ^{α}/g^{α} much different than unity in the above formulation,

$$\dot{\gamma}^{\alpha} = \begin{cases} \dot{\gamma}_0^{\alpha} \left[\left(\frac{\tau^{\alpha}}{g^{\alpha}} \right)^{\frac{1}{m}} - 1 \right] & \tau^{\alpha} \geq g^{\alpha} \\ 0 & \tau^{\alpha} < g^{\alpha} \end{cases} \quad (2.13)$$

This expression differentiates between the positive and negative slip direction and slip plane normal pairs, $\pm \bar{\mathbf{s}}^{\alpha} \otimes \bar{\mathbf{m}}^{\alpha}$, constraining the slip rate to be nonnegative.

Hence, the slip only occurs for $\tau^\alpha > g^\alpha$. Note that this modification also avoids the singularity at $\tau^\alpha = g^\alpha$, leading to zero slip velocity.

For multiple slip, the rate of the shear flow stresses is governed by a diagonal hardening law based on statistical mechanics:

$$\dot{g}^\alpha = \sum_{\beta} h^{\alpha\beta} \dot{\gamma}^\beta \quad (2.14)$$

where $h^{\alpha\alpha}$ are the diagonal hardening moduli:

$$h^{\alpha\alpha} = 2h_c(t) \left[\frac{\tau_c^\alpha(t)}{\tau_c^\alpha(t)} \right]^3 \left\{ \cosh \left[\left(\frac{\tau_c^\alpha(t)}{\tau_c^\alpha(t)} \right)^2 \right] - 1 \right\} \quad \text{no sum in } \alpha \quad (2.15)$$

In the above expression,

$$\tau_c^\alpha(t) = a\mu b\sqrt{\pi n^\alpha(t)} \quad \text{and} \quad h_c(t) = \frac{\tau_c^\alpha(t)}{\gamma_c^\alpha(t)} \quad \text{no sum in } \alpha \quad (2.16)$$

are a characteristic shear stress and plastic modulus, respectively. These values determine the location of the bend in the resolved shear stress-slip strain curve. In equation 2.16, μ is the shear modulus, b is the Burgers vector, a is a coefficient of the order of 0.3 that regulates the strength of the obstacle, ρ^α is the dislocation density and n^α is the density of obstacles in slip system α . The hardening moduli, $h^{\alpha\alpha}$, introduced by this model is based on two complementary models, models of Pierce *et al.* [44] and Bassani and Wu [4]. The model of Pierce *et al.* suggests a hardening moduli in the form below

$$h^{\alpha\beta} = h(\gamma)(q + (1 - q)\delta^{\alpha\beta}) \quad (2.17)$$

where γ is the sum of the slip strains on all slip systems. The parameter q characterizes the hardening behavior, $q = 1$ corresponding to isotropic or Taylor hardening. For FCC metals, Kocks [28] determined the range of this parameter to be $1 < q \leq 1.4$. A form of $h(\gamma)$ suitable for Al-Cu alloys is introduced by Chang and Asaro [10]

$$h(\gamma) = h_0 \text{sech}^2\left(\frac{h_0\gamma}{\tau_s - \tau_0}\right) \quad (2.18)$$

where h_0 is the initial hardening rate, τ_0 is the critical resolved shear stress and τ_s is the saturation strength. The model of Bassani and Wu proposed a model of hardening

in single crystals in which the hardening moduli are in the below form

$$h_{\alpha\alpha} = \left[(h_0 - h_s) \operatorname{sech}^2 \left(\frac{(h_0 - h_s) \gamma_\alpha}{\tau_I - \tau_0} \right) + h_s \right] \left[1 + \sum_{\substack{\beta=N \\ \beta \neq \alpha}} f_{\alpha\beta} \tanh \left(\frac{\gamma_\beta}{\gamma_0} \right) \right] \quad \text{no sum on } \alpha \quad (2.19)$$

$$h_{\alpha\beta} = \epsilon h_{\alpha\alpha} \quad \alpha \neq \beta \quad \text{no sum on } \alpha \quad (2.20)$$

where τ_I is the stage I stress, the threshold stress at which large plastic flow starts, h_0 and h_s define the hardening slope immediately following initial yield and during easy glide, respectively and ϵ is a parameter that defines the off-diagonal terms, i.e., $\epsilon = 0$ is the diagonal form of the hardening moduli. The latent hardening is predicted to occur by the dislocation model as follows. During the initial single slip regime, the dislocation multiplication takes place on the primary slip system. The number of point obstacles on the primary system remains relatively small and the deformation proceeds by easy glide. At the same time, point obstacles on the secondary systems grows rapidly due to dislocation multiplication on the primary system. The hardening coefficient, $a^{\alpha\beta}$, influences the rates of multiplication which raises the critical stresses on the secondary systems even though yield stress remains small on the secondary slip system. The discrepancies between these two theories (Pierce *et al.* and Bassani and Wu) regarding the form of the hardening matrix come largely from the definition of flow stress adopted. If the emphasis is on τ_c^β , which corresponds to the back-extrapolation definition of the flow stress, then the hardening matrix is non-diagonal. If, on the contrary, the variation of the yield stress is sought as in the model of Bassani and Wu, then a diagonal hardening matrix becomes appropriate. Cuitiño and Ortiz [12] explains that these two models outlined are complementary, rather than contradictory.

2.3 Self-Hardening

In this section, the hardening relations of ductile crystals from dislocations mechanics is explained. The motion of dislocations will be considered within a generic slip system. This is the main mechanism of interactions between moving dislocations and secondary dislocations piercing the slip system. This elaborate interplay is driven by the resolved shear stress on the slip plane which is caused by the overall force applied to the model.

Because of the random nature of the interactions, the best description comes from statistical models.

The strength of the obstacle in the slip plane α , created by a pair of forest dislocations separated by a distance l , can simply be estimated as

$$s^\alpha = a \frac{\mu b}{l} \quad (2.21)$$

Above equation is obtained using line tension calculations, see for example Kovács and Zsoldos [31]. The central assumption in forest theory of hardening is that, for high-purity single crystals, the main resistance to dislocation motion is forest dislocations, described as the secondary dislocations piercing the slip plane. Forest dislocations can be visualized as point obstacles that are effective over only a few atomic distances. Pairs of such point obstacles avoid dislocations from moving further unless a certain threshold resolved shear stress is reached, as shown in figure 2.1.

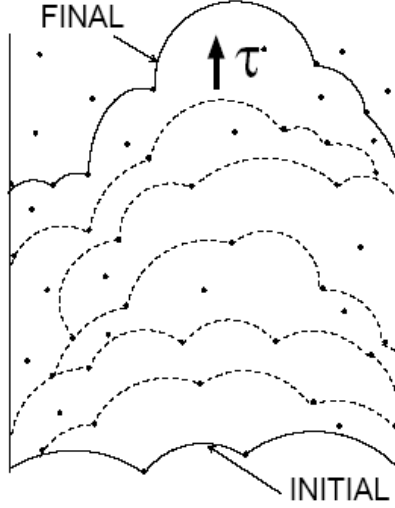


Figure 2.1: Dislocation passing through a randomly distributed point obstacles under monotonic loading

If locations of the point obstacles are assumed to be completely uncorrelated and that the pairs of points defining a barrier are next neighbors, the probability density function for next distances becomes [27]

$$\tilde{f}(l, t) = 2\pi n(t) l e^{-\pi n(t) l^2} \quad (2.22)$$

where $n(t)$ is the area density of forest dislocation intersections with the glide plane at time t . Using 2.21 to change variables, we can define the probability density function of two-point barrier strength s at time t as

$$\tilde{f}(s, t) = \frac{2\pi n(t)(\alpha\mu b)^2}{s^3} e^{-\pi n(t)(\frac{\alpha\mu b}{s})^2} \quad (2.23)$$

The time dependence of $\tilde{f}(s, t)$ is a consequence of the variation in forest dislocation density.

We can start explaining the interactions between a moving dislocation and the distributed point obstacles, strictly restricted to the case of rate-independent and monotonic loading, by defining a resolved shear stress acting on the slip system at time t , $\tau(t)$. Evidently, for dislocations to be arrested at time t , they must face barriers of strength s which is higher than $\tau(t)$. As $\tau(t)$ is increased to $\tau(t) + \dot{\tau}(t)dt$, the dislocation segments stuck at barriers of strength ranging from $\tau(t)$ to $\tau(t) + \dot{\tau}(t)dt$ are released and move forward until a higher barrier strength is reached, figure 2.1. This mechanism of dislocation movement results in an incremental increase in the plastic deformation.

Ortiz and Popov [42] noted that the information needed to describe the dislocation motion is contained in the probability density function, $f(s, t)$, which stands for the fraction of dislocation length facing barriers of strength s at time t . At $t = 0$, the dislocation s may be assumed to be randomly distributed over the slip plane, and

$$f(s, 0) = \tilde{f}(s, 0) \quad (2.24)$$

The probability that an unstable dislocation segment moves to a barrier of a stronger obstacle pair is given by

$$\tilde{f}(s'|s' > \tau(t)) = \frac{\tilde{f}(s', t)H(s' - \tau(t))}{1 - \tilde{P}(\tau(t), t)} \quad (2.25)$$

where H is the Heaviside step function and $\tilde{P}(\tau(t), t)$ is the distribution function. Thus, the dislocation segments redistribute themselves proportionally to $\tilde{f}(s', t)$ over admissible interval $[\tau(t), \infty]$. Consequently, the transition probability rate that a dislocation segment moves from a barrier of strength s to another of strength s is given by

$$\psi(s \rightarrow s', t) = \frac{\tilde{f}(s', t)H(s' - \tau(t))}{1 - \tilde{P}(\tau(t), t)} \delta(s - \tau(t)) \dot{\tau}(t) \quad (2.26)$$

Because of the Markovian nature of the dislocation flights, the evolution of $f(s, t)$ is governed by Pauli's master equation

$$\frac{\partial f(s, t)}{\partial t} = \int_0^\infty [\psi(s' \rightarrow s, t)f(s', t) - \psi(s \rightarrow s', t)f(s, t)]ds' + g(s, t) \quad (2.27)$$

where $g(s, t)$ describes the rate of variation of $f(s, t)$ due to external agencies and in the absence of transitions. For the system considered, $g(s, t)$ represents the rate of change of $f(s, t)$ due to the evolution of barrier strength probabilities, $\tilde{f}(s, t)$. As noted earlier, the main variable in the latter evolution is the density of the forest dislocations, $n(t)$. Evaluation of $g(s, t)$ can be explained by freezing $\tau(t)$ at its current value and suppose that $\tilde{f}(s, t)$ changes to $\tilde{f}(s, t + dt)$. This approach can be understood by regarding all dislocation segments as stably pinned at their current locations while adding or removing point obstacles from the considered slip plane. Some of these new obstacles arrest the dislocation lines and thus, a change in $f(s, t)$ occurs. The probability that a segment comes to face a new barrier of strength s is proportional to $f(s, t)$. Therefore, the rate at which $f(s, t)$ changes due to this mechanism is

$$g(s, t) = \frac{\partial}{\partial t} \left[\frac{\tilde{f}(\tau, t)}{1 - \tilde{P}(\tau, t)} H(s - \tau) \right]_{\tau=\tau(t)} \quad (2.28)$$

Inserting equations 2.26 and 2.28 into equation 2.27 the equation of evolution arrives at

$$\begin{aligned} \frac{\partial f(s, t)}{\partial t} = & \left[\frac{\tilde{f}(s, t)H(s - \tau(t))}{1 - \tilde{P}(\tau(t), t)} - \delta(s - \tau(t)) \right] f(\tau(t), t)\dot{\tau}(t) \\ & + \frac{\partial}{\partial t} \left[\frac{\tilde{f}(\tau, t)}{1 - \tilde{P}(\tau, t)} H(s - \tau) \right]_{\tau=\tau(t)} \end{aligned} \quad (2.29)$$

The above equation may be viewed as a statement of gains and losses. The Dirac-delta term on the right hand side has the effect of removing probability density from the interval $\tau(t) \leq s \leq \tau(t) + \dot{\tau}(t)dt$ while the remaining terms in the bracket distributes it over the interval $[\tau(t), \infty]$ proportionally to $\tilde{f}(s, t)$ as in figure 2.2. When the slip system remains unloaded at all times, equation 2.29 becomes $f(s, t) = \tilde{f}(s, t)$, $t \geq 0$. This should indeed be the case in the absence of applied stress. The dislocation lines remain randomly distributed over the slip plane and, consequently, the probability that a dislocation line segment face a barrier of strength s is necessarily equal to $\tilde{f}(s, t)$.

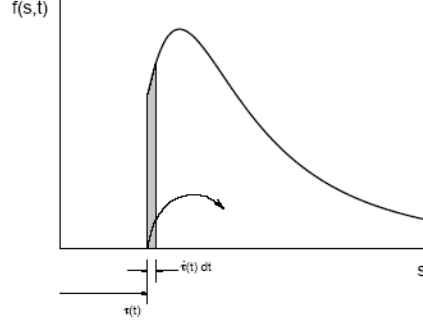


Figure 2.2: Redistribution of the probability density $f(s, t)$ upon a resolved shear stress increment

The kinetic equation 2.29 admits the simple closed form solution

$$f(s, t) = \frac{\tilde{f}(s, t)H(s - \tau(t))}{1 - \tilde{P}(\tau(t), t)} \quad (2.30)$$

which is only valid for monotonically increasing $\tau(t)$ only. Solution 2.30 implies that the probability density $f(s, t)$ remains proportional to $\tilde{f}(s, t)$ over the current admissible range $[\tau(t), \infty]$. Equation 2.30 fully characterizes the self-hardening of a slip system.

Now, we can proceed to calculate the slip rate, $\dot{\gamma}(t)$, instigated by the dislocation motion. The dislocation density released during an increment of the resolved shear stress causes an incremental plastic strain ([27]). Let $\rho(t)$ denote the current dislocation length per unit volume for the slip system, then slip rate can be found as

$$d\gamma(t) = b\rho(t)f(\tau(t), t)\dot{\tau}(t)dt\bar{N}(t)\bar{l}(t) \quad (2.31)$$

where $\bar{l}(t)$ is the average distance between barriers, and $\bar{N}(t)$ is the average number of jumps the dislocation segments make before reaching stability.

$\bar{l}(t)$ can be approximated as the average distance, $\langle l \rangle(t)$, between point obstacles and $\bar{l}(t) = \langle l \rangle(t) = \frac{1}{2\sqrt{n(t)}}$ can be obtained. Next, we need to compute the average number of jumps, $\bar{N}(t)$. The probability that an moving dislocation segment gets pinned after the first jump is equal to the probability that the first barrier faced is of strength $s \geq \tau(t)$ which is $1 - \tilde{P}(\tau(t), t)$. Evidently, the probability that the segment moves without being tackled by the first encounter is $\tilde{P}(\tau(t), t)$. For the second barrier, the corresponding probabilities are $\tilde{P}(\tau(t), t)[1 - \tilde{P}(\tau(t), t)]$ and $\tilde{P}^2(\tau(t), t)$, respectively.

Hence, the average number of jumps taken by unstable segment before being arrested is

$$\begin{aligned}\bar{N}(t) &= [1 - \tilde{P}(\tau(t), t)] + 2\tilde{P}(\tau(t), t)[1 - \tilde{P}(\tau(t), t)] + 3\tilde{P}^2(\tau(t), t)[1 - \tilde{P}(\tau(t), t)] \\ &= \frac{1}{1 - \tilde{P}(\tau(t), t)}\end{aligned}\tag{2.32}$$

Equation 2.32 gives $\bar{N} = 1$ when $\tau = 0$ and, gives $N = \infty$ when $\tilde{f}(s, t)$ has bounded support, i.e. $[0, s_{max}(t)]$, for which $\tau(t) > s_{max}(t)$, as expected. Substituting equations 2.32 and 2.30 into 2.31 with $s = \tau^+(t)$, we obtain

$$\dot{\gamma}(t) = \gamma_c(t) \frac{\tilde{f}(\tau(t), t)}{[1 - \tilde{P}(\tau(t), t)]^2} \dot{\tau}(t)\tag{2.33}$$

where the characteristic plastic strain is defined as

$$\gamma_c(t) = b\rho(t)\bar{l}(t)\tag{2.34}$$

It should be noted that 2.33 is explicit in $\tilde{f}(s, t)$ and $\rho(t)$. The former is given by equation 2.23 and the corresponding distribution function

$$\tilde{P}(s, t) = \exp\left[-\pi n(t)\left(\frac{\alpha\mu b}{s}\right)^2\right]\tag{2.35}$$

once the point obstacle density $n(t)$ is known. This, in turn, is a function of dislocation densities in the remaining slip systems. The precise form of this dependence will be obtained in the next section.

Equation 2.33 can be simplified as

$$\dot{\gamma}(t) = \frac{\dot{\tau}(t)}{h(t)}\tag{2.36}$$

where $h(t)$ is the self-hardening modulus of the slip system and can easily be obtained from equation 2.33

$$\dot{\gamma}(t) = \frac{\dot{\tau}(t)}{h(t)}\tag{2.37}$$

The effect of slip in one system on the hardening parameters of the rest of the slip planes is presumed to be contained in dislocation density n^α . The experimental work of Franciosi and co-workers [19, 20, 16, 15, 18] suggests a dependence of the form

$$\frac{1}{h(t)} = \gamma_c(t) \frac{\tilde{f}(\tau(t), t)}{[1 - \tilde{P}(\tau(t), t)]^2}\tag{2.38}$$

This formula is valid for any assumed distribution of barrier strengths. $\tilde{f}(s, t)$ provided as in equation 2.23, then the self hardening modulus is found to be

$$h(t) = h_c(t) \frac{2\tau^3(t)}{\tau_c^3(t)} \left[\cosh \left(\frac{\tau_c^2(t)}{\tau^2(t)} \right) - 1 \right] \quad (2.39)$$

where

$$\tau_c(t) = \alpha \mu b \sqrt{\pi n(t)}, \quad h_c(t) = \frac{\tau_c(t)}{\gamma_c(t)} \quad (2.40)$$

are a characteristic shear stress and plastic modulus, respectively. The values of τ_c and γ_c determine the location of the ‘bend’ in the resolved shear stress-slip strain curve. The hardening modulus decreases monotonically to zero as τ is increased.

In the present rate-independent framework, we no longer assume that the loading is monotonic, but continue to require that $\tau(t)$ not change sign throughout loading. Define the current flow stress $g(t)$ of the slip system as

$$g(t) = \max(\tau(s)), \quad s \in [0, t] \quad (2.41)$$

which is

$$\dot{g}(t) = \begin{cases} \dot{\tau}(t), & \text{if } \tau(t) = g(t) \text{ and } \dot{\tau}(t) \geq 0 \\ 0 & \text{otherwise} \end{cases} \quad (2.42)$$

in rate form. $g(t)$ is defined to be the maximum attained resolved shear stress on the slip system. Because $f(s, t)$ vanishes in the interval $[0, g(t)]$ acts as an induced elastic domain. Any part of the loading history contained in $[0, g(t))$ leaves γ and g unchanged. Consider the case when $\tau(t) = g(t)$ but $\dot{\tau}(t) = 0$ which leads to $\dot{g}(t) = 0$. The model requires that the dislocation segments be pinned at obstacles of strength greater or equal to the previously attained maximum resolved shear stress. Therefore, the stresses in the range $[0, g(t))$ are not capable of causing further dislocation motion. Now, we can rewrite the equations 2.33 and 2.38 as

$$\dot{\gamma}(t) = \frac{\dot{g}(t)}{h(t)}, \quad \frac{1}{h(t)} = \gamma_c(t) \frac{\tilde{f}(g(t), t)}{[1 - \tilde{P}(g(t), t)]^2} \quad (2.43)$$

2.4 Cross-Hardening

In the present theory we have explained so far the short range relationships on the slip systems determine the rate of self-hardening of a slip system. A key variable in the description of self-hardening is the density of point obstacles caused by forest dislocation, n^α , which is clearly a function of the dislocation densities in all the remaining systems. Franciosi and co-workers [19, 15, 18, 16, 17, 20] suggested a relationship between density of point obstacles in slip system, say α , and dislocation densities on all of the remaining slip systems, say β

$$n^\alpha = \sum_{\beta} a^{\alpha\beta} \rho^\beta \quad (2.44)$$

Franciosi and Zaoui [20] also experimentally determined values of the interaction matrix, $a^{\alpha\beta}$, for the 12 slip systems belonging to the family of $\{111\}$ planes and $[110]$ directions in FCC crystals. The interactions are classified according to whether the dislocations

- belong to the same system (Self Hardening (SH), interaction coefficient a_0)
- fail to form junctions (Coplanar systems (Copl), int. coeff. a_1)
- form Hirth locks (Hirth lock systems (HL), int. coeff. a_1)
- form Colinear junctions (Colinear systems (CL), int. coeff. a_1)
- form Glissile junctions ((GJ), int. coeff. a_2)
- form sessile Lomer-Cottrell locks (Lomer-Cottrell sessile locks (LC), int. coeff. a_3)

with $a_0 \leq a_1 \leq a_2 \leq a_3$. Franciosi [17] also found that the interaction coefficients are linearly dependent on the stacking fault energy of the crystal and the degree of anisotropy increases with decreasing stacking fault energy. Franciosi and Zaoui [20] tabulated their findings on the interaction coefficient as in table 2.1. 4 Slip planes ($\bar{1}11$), (111) , $(\bar{1}\bar{1}1)$, $(1\bar{1}1)$ are named A, B, C, D respectively and the 6 slip directions $[011]$, $[0\bar{1}1]$, $[101]$, $[\bar{1}01]$, $[\bar{1}10]$, $[110]$ are named 1 – 6 respectively.

In order to obtain a closed set of constitutive relations, equations of evolution for the dislocation densities are required. Theoretical [33] and experimental [25] studies

Table 2.1: The $|a|$ matrix

	A2	A3	A6	B2	B4	B5	C1	C3	C5	D1	D4	D6
A2	SH	Copl	Copl	CS	GJ	GJ	HL	GJ	LC	HL	LC	GJ
A3	Copl	SH	Copl	GJ	HL	LC	GJ	CS	GJ	LC	HL	GJ
A6	Copl	Copl	SH	GJ	LC	HL	LC	GJ	HL	GJ	GJ	CS
B2				SH	Copl	Copl	HL	LC	GJ	HL	GJ	LC
B4					SH	Copl	LC	HL	GJ	GJ	CS	GJ
B5						SH	GJ	GJ	CS	LC	GJ	HL
C1							SH	Copl	Copl	CS	GJ	GJ
C3								SH	Copl	GJ	HL	LC
C5									SH	GJ	LC	HL
D1										SH	Copl	Copl
D4											SH	Copl
D6												SH

shows that the dislocation production is proportional to the cross-glide multiplication.

This gives the relation

$$b\dot{\rho}^\alpha = \lambda\dot{\gamma}^\alpha \quad (2.45)$$

The coefficient λ may be interpreted as the reciprocal mean free path between cross-glide events. The rate of dislocation attrition due to pair annihilation can be expressed as (Sackett *et al.* [49])

$$b\dot{\rho}^\alpha = -\kappa\rho^\alpha\dot{\gamma}^\alpha \quad (2.46)$$

where κ may be defined as the mean radius of interaction for dislocation segment annihilation. Combining equations 2.45 and 2.46, the rate of change of dislocation density may be written as

$$\dot{\rho}^\alpha = \frac{\lambda}{b} \left(1 - \frac{\rho^\alpha}{\rho^{sat}} \right) \dot{\gamma}^\alpha \quad (2.47)$$

where $\rho^{sat} \equiv \lambda/\kappa$ is a saturation density where rate of annihilation balances the rate of production. Finally, a relation that places the dislocation density, ρ^α , and slip strain in one-to-one correspondence can be postulated. The resulting expression is given by

$$\rho^\alpha = \rho^{sat} \left[1 - \left(1 - \frac{\rho_0^\alpha}{\rho^{sat}} \right) e^{-\gamma^\alpha/\gamma_{sat}} \right] \quad (2.48)$$

where ρ_0^{sat} and $\gamma_{sat} \equiv b\rho_{sat}/\lambda$ are the initial dislocation density in system α and saturation shear strain. It should be noted that the mobile and immobile dislocations are not differentiated explicitly in the above expression. ρ^α denotes total dislocation density (i.e., mobile and immobile). The fraction of the dislocation density contributing to the plastic strain rate, $\dot{\gamma}^\alpha$, is determined by the probability density function $f(s, t)$.

2.5 Summary of the Constitutive Relations

We have completed the relations defining the dislocation model. We have started by modeling the motion of a dislocation line through forest dislocation by a statistical approach, followed by formulation of the short range interactions between pairs of dislocations and the resulting strength. We have formed relations for self hardening and cross hardening. The resulting constitutive framework is summarized below.

$$\begin{aligned}
 \dot{\gamma}^\alpha &= \phi(\tau^\alpha, g^\alpha) = \begin{cases} \dot{\gamma}_0 \left[\left(\frac{\tau^\alpha}{g^\alpha} \right)^{\frac{1}{m}} - 1 \right] & \tau^\alpha \geq g^\alpha \\ 0 & \text{otherwise} \end{cases} \\
 \dot{g}^\alpha &= h^{\alpha\alpha} \dot{\gamma}^\alpha \\
 h^{\alpha\alpha} &= h_c^\alpha \left(\frac{g^\alpha}{\tau_c^\alpha} \right)^3 \left\{ \cosh \left[\left(\frac{\tau_c^\alpha}{g^\alpha} \right)^2 \right] - 1 \right\} \\
 h_c^\alpha &= \frac{\tau_c^\alpha}{\gamma_c^\alpha}, \quad \tau_c^\alpha \equiv \alpha \mu b \sqrt{\pi n^\alpha}, \quad \gamma_c^\alpha \equiv \frac{b \rho^\alpha}{2 \sqrt{n^\alpha}} \\
 n^\alpha &= \sum_\beta a^{\alpha\beta} \rho^\beta \\
 \rho^\alpha &= \rho^{sat} \left[1 - \left(1 - \frac{\rho_0^\alpha}{\rho^{sat}} \right) e^{-\gamma^\alpha / \gamma^{sat}} \right]
 \end{aligned}$$

Table 2.2: Constitutive model parameters for pure aluminum

Parameter	Value	Parameter	Value
C_{11}	108 GPa	C_{22}	61 GPa
C_{44}	28.5 GPa	g_0	38 MPa
a_0	7.5×10^{-4}	a_1/a_0	2.25
a_2/a_0	4	a_3/a_0	5
S	$135 \times 10^{-3} \text{ J } m^{-2}$	m	0.1
$\dot{\gamma}_0$	10 s^{-1}	γ^{sat}	0.1%
ρ_0	$10^{16} m^{-2}$	ρ^{sat}	$5.5 \times 10^{16} m^{-2}$
b	2.56×10^{-10}		

Chapter 3

Sensitivity Analysis

3.1 Introduction

The purpose of computational models and simulations is to reflect the actual responses of materials and capture the important parameters as accurate as possible. Before attempting to obtain important manufacturing parameters, the computational model introduced should be checked for its response to some typical and easily observable parameters. We will call this procedure *sensitivity analysis*. Sensitivity analysis of the predicted results should be undertaken with respect to all assumptions or approximations used in the model. In this chapter, we will try to explain how the changes in these parameters, listed below, affect certain behaviors of the material, Al alloy 6022-T43. These behaviors are already observed or experimented by researchers and the sole purpose of this chapter is to verify these responses and confirm that the material model functions as expected.

Five parameters, namely *initial yield stress* (g_0), *initial dislocation density* (ρ_0), *saturation dislocation density* (ρ_{sat}), *self hardening parameter* (a_0) and *saturation shear strain* (γ_{sat}) is set to several different values to obtain stress-strain behaviors, r-values, dislocation densities, and active slip systems of the aluminium sample. During the trials, the response for the changes in the above mentioned parameters are collected and analyzed to understand the effect of the parameters. The parameters were changed up and down in the order of magnitude and depending on the observation further trials were conducted. 100 orientations are used to conduct the simulations. The method of selection of the particular 100 orientations are described in the following chapter.

Alcoa's experimental research, [8], supplied the orientations after rolling obtained from x-ray diffraction. These orientations possess the texture evolution during

rolling (hydraulic bulge test system). In the hydraulic bulge test, a sheet metal test specimen is bulged by a hydraulic medium. The geometry of the bulged test specimen is defined by the geometry of the bulge die. The test provides rapid biaxial stress-strain curve of sheet material and biaxial tensile strain limits of the materials. Figure 3.1 shows the geometric parameters of the test.

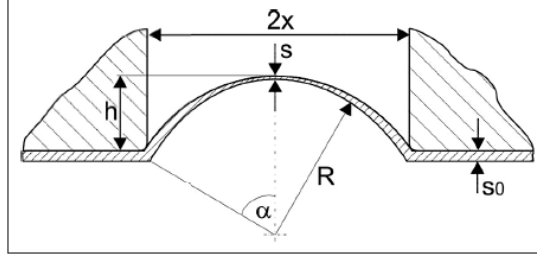


Figure 3.1: Geometric parameters of the hydraulic bulge test

For the purpose of sensitivity analysis, we have used these orientations determined by x-ray diffraction resulted by the hydraulic bulge test conducted. The reader should note that the analysis conducted in this chapter and chapter 4 are different than chapter 5. While the current chapter and chapter 4 involves the simulation of only uniaxial tensile test with experimental orientations, chapter 5 accommodates both rolling and uniaxial simulations starting from randomly generated 1000 orientations or selected 100 orientations from a random set of 1000 orientations. The reader should also note that the boundary conditions of the hydraulic bulge test is somewhat different than a regular rolling operation where the edges of the sheet material are free along the rolling direction rather than clamped at all directions as in hydraulic bulge test. The following equations are once again emphasized for the ease of following the work explained in this chapter. The details of these equations are supplied in chapter 2.

$$\rho^\alpha = \rho_{sat} \left[1 - \left(1 - \frac{\rho_0^\alpha}{\rho_{sat}} \right) e^{-\gamma^\alpha / \gamma_{sat}} \right] \quad (3.1)$$

$$n^\alpha = \sum_{\beta} a^{\alpha\beta} \rho^\beta \quad (3.2)$$

$$\dot{\gamma}^{\alpha} = \begin{cases} \dot{\gamma}_0^{\alpha} \left[\left(\frac{\tau^{\alpha}}{g^{\alpha}} \right)^{\frac{1}{m}} - 1 \right] & \tau^{\alpha} \geq g^{\alpha} \\ 0 & \tau^{\alpha} < g^{\alpha} \end{cases} \quad (3.3)$$

3.2 Initial Yield Stress

Initial yield stress (g_0) defines the amount of current shear flow stress (g^{α}) to be reached to start the plastic deformation. Once the current shear flow stress in individual slip systems reach initial yield stress, the polycrystal will start plastic deformation subsequently. A behavior similar to a response to changing yield stress values in the classical understanding of mechanics of materials can be observed with changes in initial yield stress. Any increase in initial yield stress directly reflects as a shift upwards in the bending point in the stress-strain curve which clearly shows that the mobilization of dislocations are harder for increased values of the parameter. As can be seen in figure 3.3 the simulations with lower initial yield stress respond faster to the uniaxial strain applied due to easier propagation of dislocations. Lower initial yield stress also causes the r-values stabilize faster with increasing strain. Low initial yield stress activates the available dislocations with leaving no available secondary dislocations to activate with higher resolved shear stress. For FCC materials every configuration has 12 slip systems. Figure 3.4 shows the percentage of active slip systems versus strain. Approximately 50% of the slip systems are active within 1% strain, with lower initial yield stress, as opposed to 25% and less than 1% with higher initial yield stress, $1.9e8$ and $3.8e8$, respectively. 72% of the slip systems are active when the sample reaches 28% total strain, more than two-thirds of the slip starting before 1% strain reached. Figure 3.4 also shows very similar slip activation for initial yield stresses of $3.8e8$ and $1.9e8$ which reflects to the r-values as can be seen in figure 3.3. Average slip rates for higher initial yield stress at the slip planes are also remarkably lower than that of lower initial yield stress parameters. Figure 3.5 shows the average of dislocation density for all of the 100 orientations used for simulations. The saturation dislocation density is $5.5e16$ and the initial dislocation density is $1.0e16$ for all of the samples in figure 3.5.

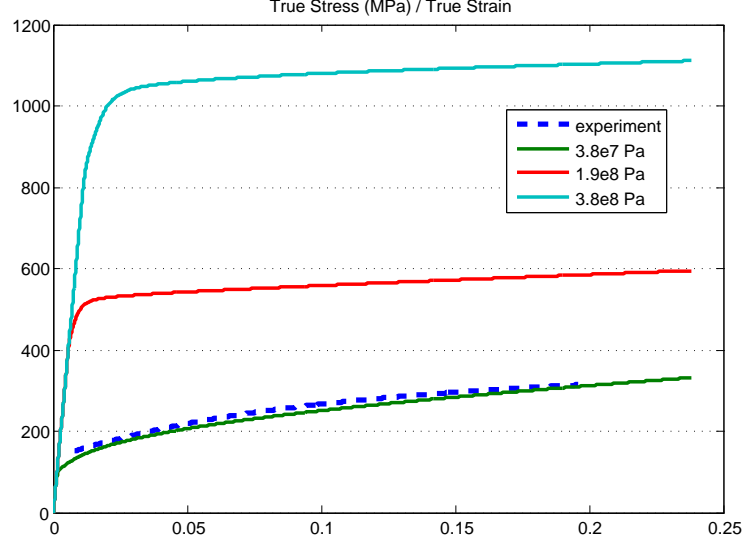


Figure 3.2: True Stress vs. True Strain with varying initial yield stress

3.3 Initial and Saturation Dislocation Density

Initial dislocation density (ρ_0) determines the density of the dislocations at the virgin state of the material, before any manufacturing or curing is applied whereas *saturation dislocation density* (ρ_{sat}) is the upper bound of dislocation density in the material while deformed. Any manufacturing process on raw material will increase the dislocation density starting from the initial dislocation density and eventually reaching saturation dislocation density if not disturbed. An increase in the initial dislocation density causes an increase in the dislocation density as defined by equation 3.1. It should be noted that equation 3.1 does not differentiate explicitly between mobile and immobile dislocation densities. The expression denotes the total dislocation density. The central assumption in the forest theory of hardening suggests that, for high-purity single-phase crystals, the main resistance to dislocation motion is posed by secondary dislocations piercing the slip plane, namely forest dislocations. These secondary dislocations create point obstacles in the primary plane and act as immovable joints creating barriers which significantly impede the dislocation motion. The increasing overlap between the strain fields of adjacent dislocations gradually increases the resistance to further dislocation motion. Pairs of point obstacles arrest dislocations in the particular slip plane, which

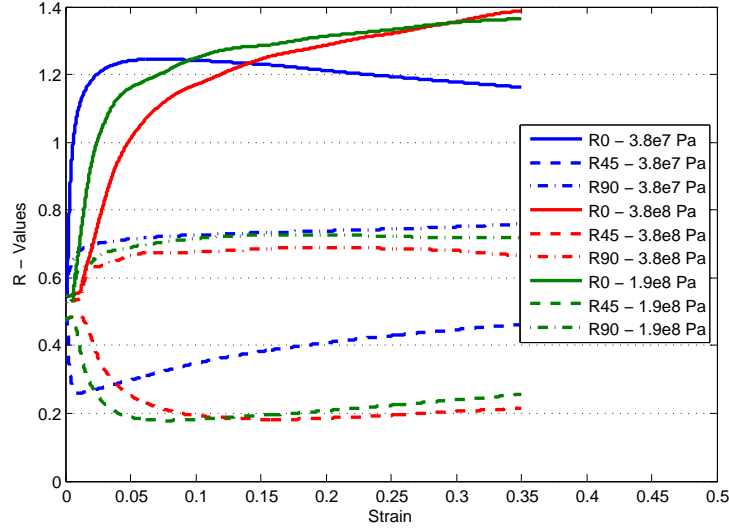


Figure 3.3: R-values vs. Strain with varying initial yield stress

require a certain threshold resolved shear stress to overcome the barrier. The value of resolved shear stress can be estimated from line tension calculations. Saturation dislocation density is a saturation density at which the rate of annihilation balances the rate of production. The effect of saturation dislocation density is also defined by equation 3.1 and an increase in the saturation dislocation density also causes an increase in the dislocation density. Increase in either ρ_0 and ρ_{sat} results with an increase in yield strength and a subsequent decrease in ductility. The effects of initial and saturation dislocation densities can be seen in figure 3.6. Equation 3.2 shows increasing dislocation density increases the number of point obstacles, shortening the distance between point obstacles which causes higher threshold resolved shear stress. The higher initial and saturation dislocation densities cause hardening due to forest dislocations and become more resistant to plastic deformation. The consequent result of increased stress at the slip planes is defined by equation 3.3 and can be observed by the simulations. Figures 3.9(a), 3.9(b), 3.10(a), and 3.10(b) depict averaged dislocation evolution, for different initial dislocation density and saturation dislocation density, latter two focusing in the initial 2.5% of strain. Average dislocation density does not reach to saturation value in any of the runs because of the nature of equation 3.1. Dislocation evolution becomes more apparent with lower initial density with forest dislocations again playing

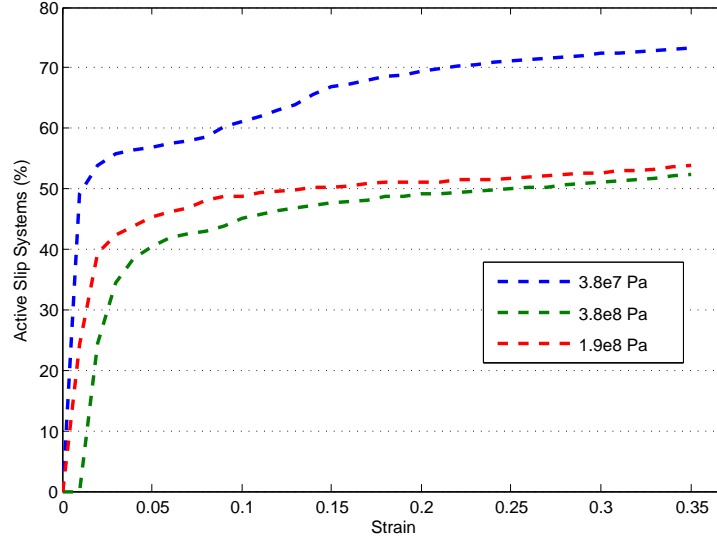


Figure 3.4: Active Slip Systems vs. Strain for varying initial dislocation density

an important role. The dislocation evolution continues until 5% of stretching as can be seen in figure 3.9(b) for two simulations with higher saturation dislocation density. The effect of longer dislocation evolution can be observed in r-values in figure 3.7(b).

3.4 Self Hardening Parameter

Self hardening parameter (a_0) simply defines the relations between slip systems and how slip systems would affect each other. FCC crystals mainly deform by crystallographic glide on $\{111\} \langle 110 \rangle$ slip systems, so that their hardening characteristics are mainly determined by the nature of the interactions between these slip systems. Equation 3.2 defines a suggestive form for dependence of point obstacles to dislocation densities in all remaining slip systems. Self hardening parameter, (a_0) defines the interactions by grading if the dislocations belong to the same system and possibility of forming point obstacles at intersecting slip planes. By changing the self hardening parameter, a_0 , and consequently a_1 , a_2 , a_3 as defined in [20], the slip systems interactions are characterized for their ability to self harden, form junctions in remaining systems. a_0 , a_1 , a_2 , a_3 are associated with interactions between dislocations that belong to the same system or stress opposing the dislocation motion, dislocations interactions on systems pairs which do not form any junction, systems pairs that form glissile junctions, systems

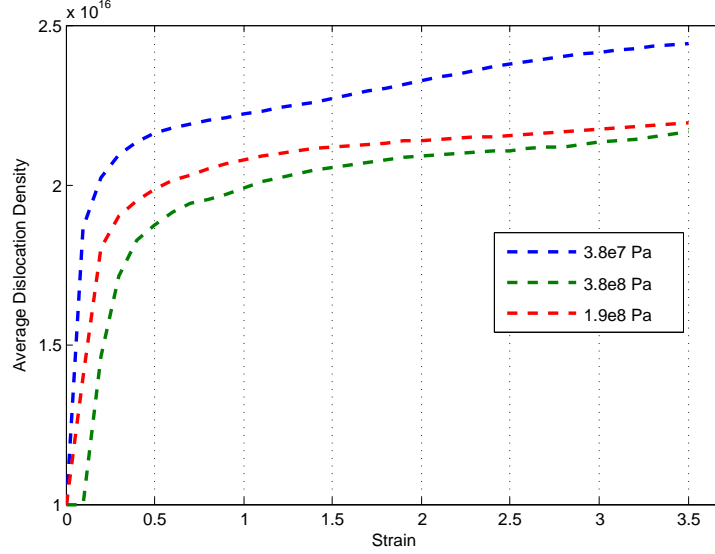
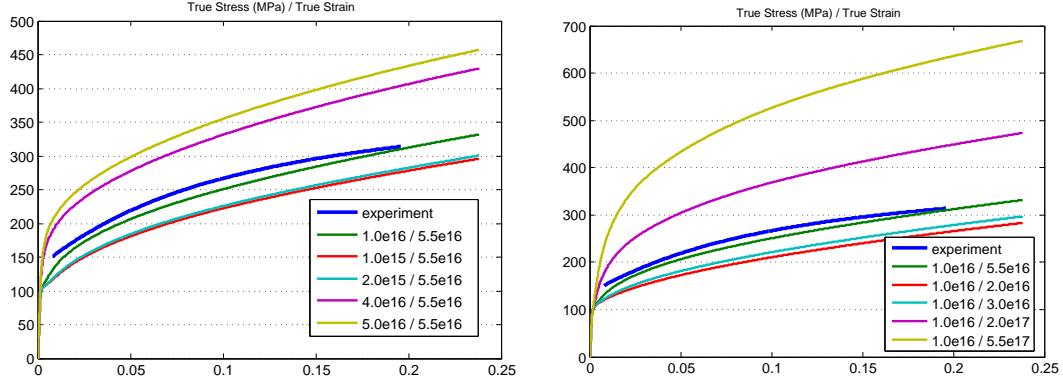


Figure 3.5: Average Dislocation Density vs. Strain with varying initial yield stress

pairs that form sessile junctions, respectively. Higher self hardening parameter defined means more dislocations belong to the same slip system and consequent resistance to dislocation motion. Figure 3.11(a) shows the resulting hardening of the sample. The a matrix anisotropy represents the strength of the contact interactions between the dislocations belonging to different slip systems. The lower is the material stacking fault energy, the more anisotropic is a . Figure 3.11(b) clearly demonstrates this course. More slip systems are activated with lower anisotropy of the interaction matrix due to less resistance caused by immobile dislocation junctions as produced by simulations (Figure 3.12(a)).

3.5 Saturation Shear Strain

Equation 3.1 defines the response of dislocation density to saturation shear strain, γ_{sat} . Higher γ_{sat} enables more deformation and causes less internal stress for the sample which explains weak hardening tendency for high γ_{sat} simulations. True stress-engineering strain curve can be viewed in figure 3.13(a) with varying material hardening. Dislocation density decreases while number of point obstacles dropping with increasing saturation shear strain. The direct effect of γ_{sat} to ρ_{sat} is given in equation 3.1 which is visible in figure 3.14(b). The impact to the anisotropy of the material is very similar



(a) True Stress vs. True Strain with varying initial dislocation densities (b) True Stress vs. True Strain with varying saturation dislocation densities

Figure 3.6: True Stress vs. True Strain with varying initial and saturation dislocation densities (Legend shows the values of initial/saturation densities)

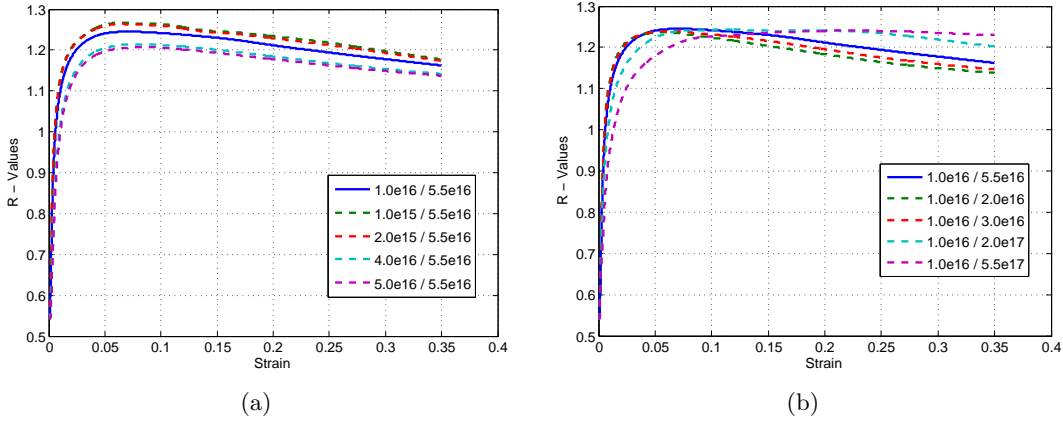


Figure 3.7: R-values vs. Strain with varying initial and saturation dislocation densities (Legend shows the values of initial/saturation dislocation densities)

to the effect of initial dislocation density, ρ_0 , and can be observed by comparing figure 3.7(a) and 3.13(b). In figure 3.14(a), it is clear that lower γ_{sat} reflect as slip systems activating quicker due to high shear stress causing arrested dislocations to break free from the barriers.

3.6 Single Slip

Lastly, the following graphs are generated to investigate the single slip behavior. Single slip refers to a single family of parallel planes that govern the changes in geometry due to disarrangements. Single slip occurs at the initial stages of deformation (approximately

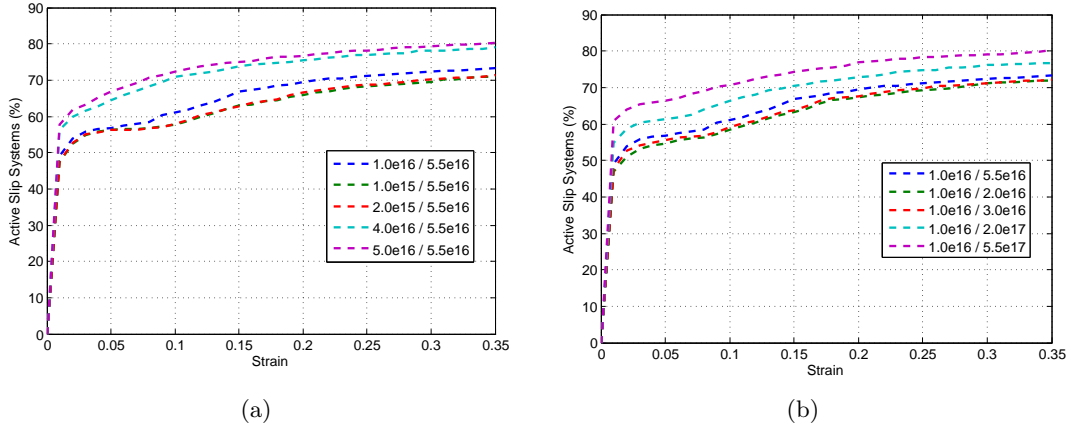


Figure 3.8: Active Slip Systems vs. Strain (Legend shows the values of initial/saturation dislocation densities)

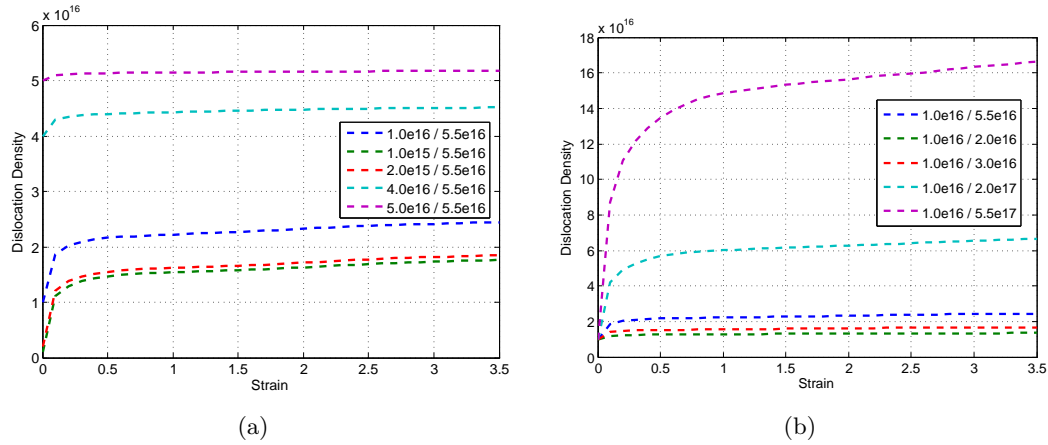


Figure 3.9: Average Dislocation Density vs. Strain (Legend shows the values of initial/saturation dislocation densities)

up to 10%) and can not be observed at the latter stages due to activities in multiple slip planes. The main parameter restricting slip is initial yield stress shown in figure 3.15(a). Slip starts at 0.5% of strain for the value of $1.9e8$, and at 1% of strain for the value of $3.8e8$. The rest of the parameters initiate the single slip around at 1% of strain. Note that, extensive single slip stage is hardly observed for the aluminum sample. The response is considered to be of a polycrystal sample in which initial stages with single slip is hardly observed for the 12 slip planes which is in agreement with the findings of [20]. This is due to relatively strong material stacking fault energy ($135e^{-3} J/m^2$) of aluminum which increases the ability of a dislocation to glide onto an intersecting slip

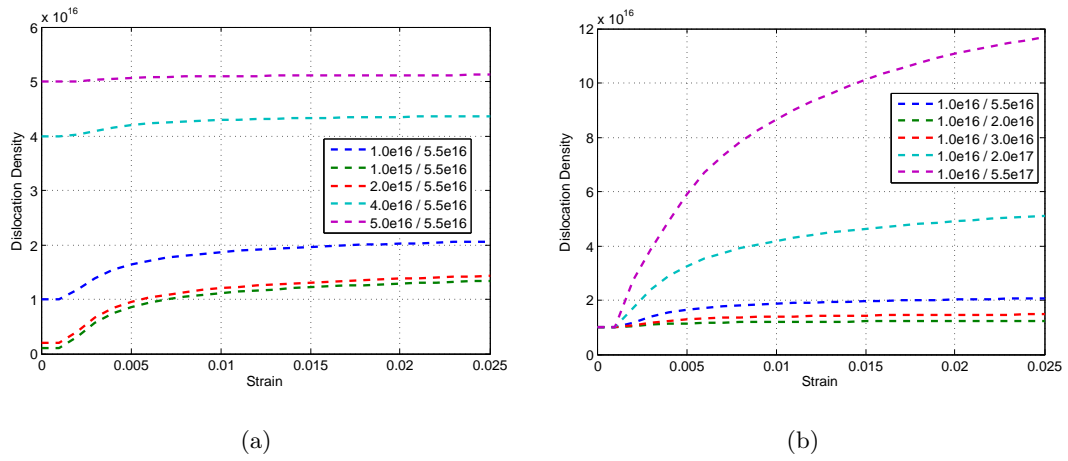
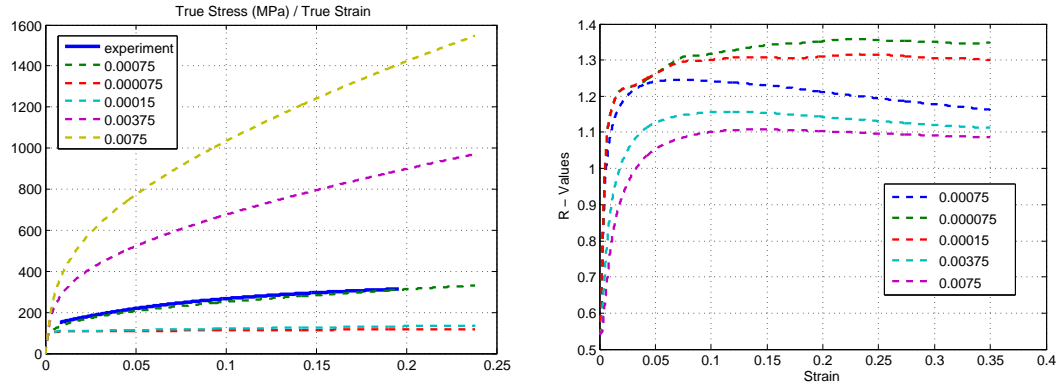


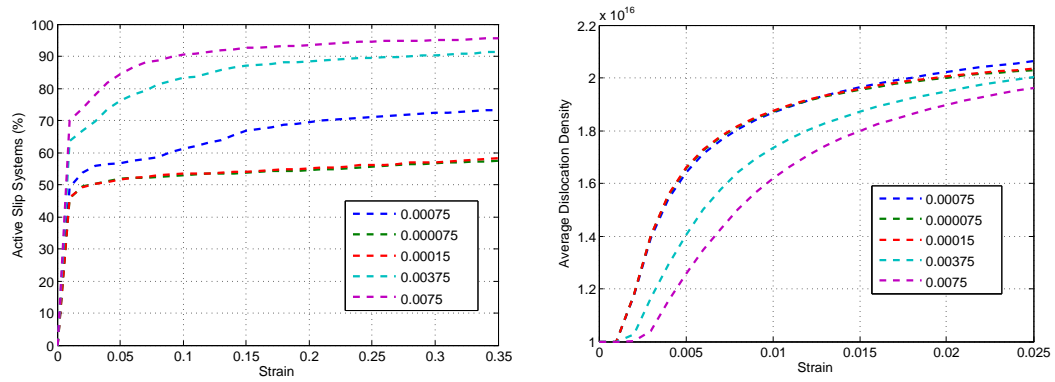
Figure 3.10: Average Dislocation Density vs. Strain for the initial stages of hardening (Legend shows the values of initial/saturation dislocation densities)

plane and causing simultaneous activation.



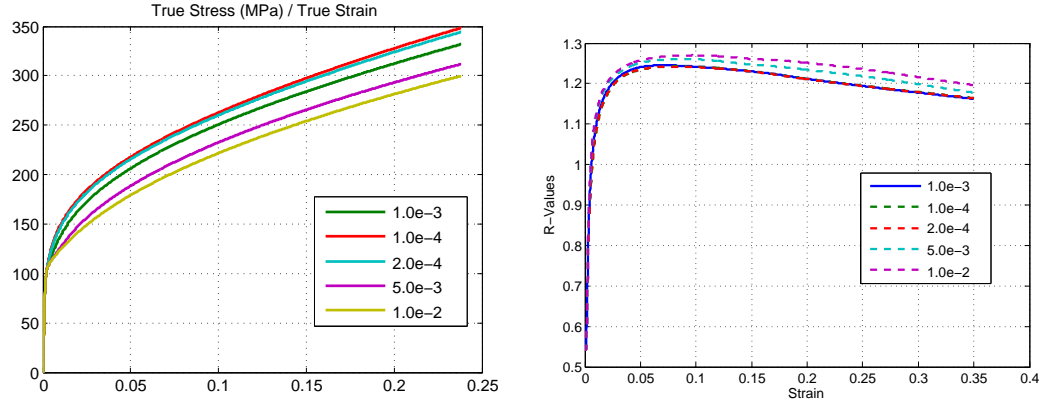
(a) True Stress vs. True Strain with varying self hardening parameter (Legend shows the values of self hardening parameter) (b) R-Values vs. Strain with varying self hardening parameter (Legend shows the values of self hardening parameter)

Figure 3.11: True stress strain graph and R - values with varying self hardening parameter



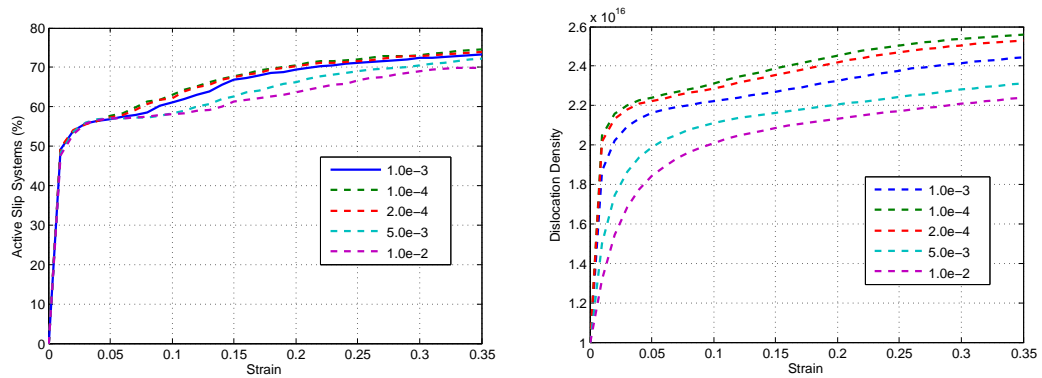
(a) Active Slip Systems vs. Strain (Legend shows the values of self hardening parameter) (b) Average Dislocation Density vs. Strain (Legend shows the values of self hardening parameter)

Figure 3.12: Active Slip Systems and Average Dislocation Density vs. Strain with varying self hardening parameter



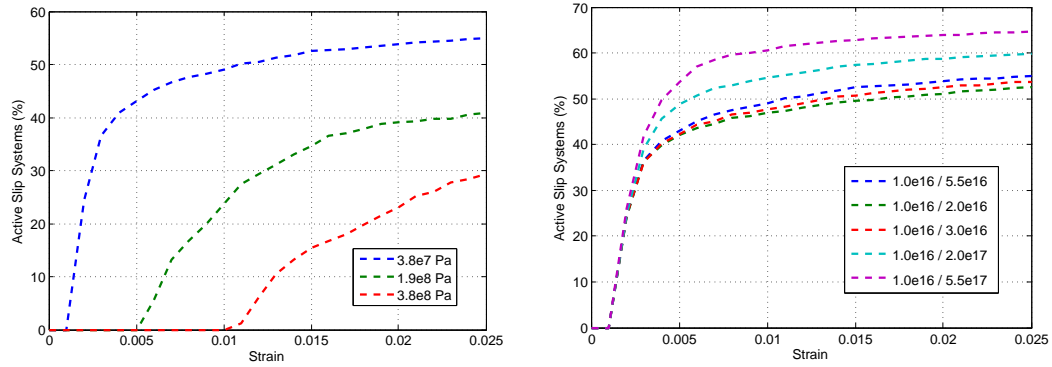
(a) True Stress vs. True Strain (Legend shows the values of saturation shear strain) (b) R-values vs. Strain (Legend shows the values of saturation shear strain)

Figure 3.13: True Stress and R-Values vs. Strain with varying self hardening parameter



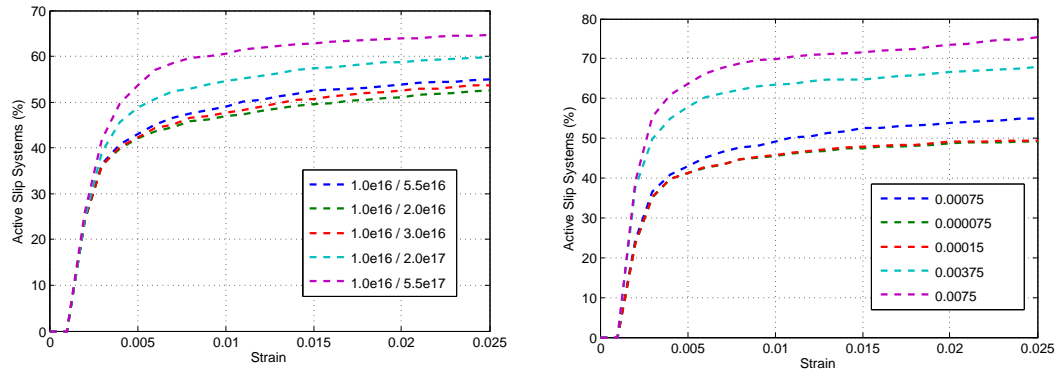
(a) Active Slip Systems vs. Strain (Legend shows the values of saturation shear strain) (b) Dislocation Density vs. Strain (Legend shows the values of saturation shear strain)

Figure 3.14: Active Slip Systems and Dislocation Densities vs. Strain with varying self hardening parameter

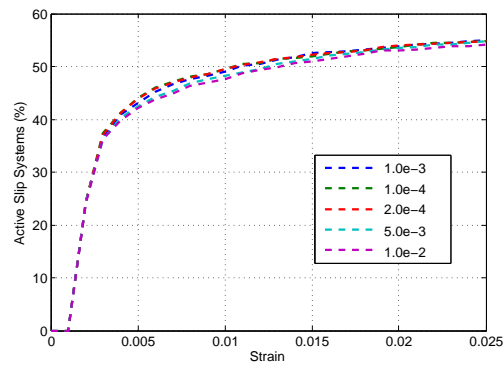


(a) Active Slip Systems vs. Strain (Legend shows the values of initial yield stress) (b) Active Slip Systems vs. Strain (Legend shows the values of initial and saturation dislocation density)

Figure 3.15: Active Slip Systems vs. Strain with varying parameters for the initial hardening stages



(a) Active Slip Systems vs. Strain (Legend shows the values of initial and saturation dislocation density) (b) Active Slip Systems vs. Strain (Legend shows the values of self hardening parameter)



(c) Active Slip Systems vs. Strain (Legend shows the values of saturation shear strain)

Figure 3.16: Active Slip Systems vs. Strain with varying parameters for the initial hardening stages

Chapter 4

Predicting R-Values

4.1 Introduction

The increasing computer power over the last few decades has changed the approach to the numerical analysis and also to the researches where computational power is indispensable. Simulations once considered impossible and impractical are now hardly time-consuming and to keep them commonplace, studies to reduce the simulation time are also considered vital and has been conducted parallel to the ongoing theoretical work. Increasing computational speed on the behavior of polycrystalline metals, of both face-centered cubic and body-centered cubic crystal structure, has also attracted additional focus.

Deformation processes in polycrystalline metals are always accompanied by a change of crystallographic orientation of each grain, which is often referred as *texture evolution*. The control of the texture evolution in metal-forming processes is of significant interest in modern industry for the purpose of specific anisotropic mechanical properties in the final products. With the advance of computational materials science in recent years, modeling and simulation has provided powerful tools both for theoretical investigations and industrial applications of texture evolution in polycrystalline metals [29].

In this paper, we present a method for the selection of orientations based on their distribution in the Euler space. The model used for the simulation is Cuitiño and Ortiz's [12] single crystal model accompanied by Taylor averaging. The single crystal model of Cuitiño and Ortiz's is a statistical mechanical model of dislocation motion through forest dislocations. Kuchnicki et al. [32] also introduced an explicit model which provides significant performance improvements. Response of the polycrystals

are based on Taylor model [52] which has been one of the most widely used approach in theoretical and industrial applications due to its simplicity. This method has been successfully used in the simulation of texture evolution in face-centered cubic [36] and body-centered cubic [30] materials. Cuitiño and Zheng [13] also introduced a formulation to apply Taylor averaging to heterogeneous foams. Taylor averaging is, however, inadequate if the crystal strength is heterogeneously distributed, like in materials with a low symmetry lattice and for poly-phase materials. It has also been observed that at large strains and in cases where the experiments show evidence of inhomogeneous deformation inside grains [40], this method tends to overpredict peak texture intensities and shift the position of texture components [22], [9]. Efficiency improvements have been proposed for industrial applications of this method [59], [60]. Recently, a numerical comparison of Taylor averaging method with low-resolution simulation (LRS) method and direct numerical simulation (DNS) method has been also investigated [58]. The results of the simulation will be compared by the experimental data supplied by Alcoa labs [8] for samples of aluminum alloys 6022-T43 ($t = 1.000\text{-mm}$).

4.2 Orientation Selection

Taylor averaging method assumes that all the grains in the sample are subjected to the same macroscopic strain. The constitutive model uses the local value of the macroscopic deformation gradient at each loading step followed by an averaging of the stress tensor. The orientations are assigned to each integration point of the mesh. Accompanied with finite element method each integration point represents the collective Taylor-averaged behavior of a large number of grain orientations. The details of the continuum finite model conducted in this work can be found in [45]. In Taylor averaging, the properties of each integration point are calculated by averaging either the stress tensor [26] or stiffness matrix [5].

We have conducted a computational simulation of a tensile test on aluminum alloy 6022-T43 which has undergone hydraulic bulge test in Alcoa Laboratories. The equal biaxial mechanical behaviors has been assessed during the test. During the hydraulic bulge test, the initial specimen has been stretched up to 51.6% of strain. The

tensile test specimens, then, taken at 0° , 15° , 30° , 45° , 60° , 75° , 90° to the rolling direction of each sheet material. Uniaxial tension tests have also been conducted on these 7 specimens. The results and the texture after the rolling process is supplied by Alcoa [8].

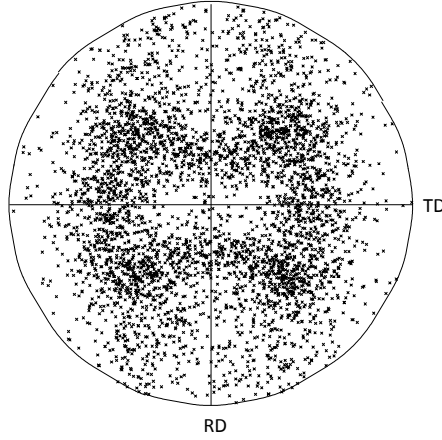
The orientation matrix is generated by 3 Euler angles. These Euler angles define a rotation matrix which orients the texture with respect to the sample coordinates. Our method uses the dispersion of Euler angles in the domain to improve the speed of the computations. The procedure used here can be summarized as:

1. Grouping of the orientations according to Euler angles
2. Picking a single orientation randomly (or choosing the median) orientations according to the dispersion of the total orientations in the generated pockets
3. Assigning weighing factors to the orientations depending on the total number of orientations in the pocket
4. During Taylor averaging use the weighing factors to calculate the overall stress

FCC crystal structure has cubic symmetry. This property restricts the range of 2 Euler angles (Φ and ϕ_2) to $0 - \pi/2$. Before allocating the appropriate space, experimentally collected Euler angles which were out of the range are recalculated to satisfy the cubic symmetry condition. Symmetry properties of the lattice is enforced during the orientation selection process to be able to group textures with close orientations.

Figure 4.1 shows the $\{111\}$ pole figure of the texture after hydraulic bulge test. In Taylor averaging, it is assumed that the local deformation gradient tensor in each grain is uniform and equal to the macroscopic deformation gradient tensor applied to the polycrystal. It should also be noted that the boundary effects are ignored. Furthermore, the Cauchy stress in the polycrystal can be taken as a simple average of the Cauchy stresses in the various grains with different orientations. Therefore, the macroscopic Cauchy stress ($\bar{\mathbf{T}}$) can be expressed as:

$$\bar{\mathbf{T}} = \frac{1}{N} \sum_{k=1}^N \mathbf{T}^{(\mathbf{k})} \quad (4.1)$$



(a) 1020 orientations

Figure 4.1: $\{111\}$ Pole figure

where N is the number of crystals in the aggregate, and T^k is the Cauchy stress in the crystal corresponding to the k th grain. In case of weighing factors included, the above formula becomes:

$$\bar{\mathbf{T}} = \frac{1}{\sum_{k=1}^N w_k} \sum_{k=1}^N w_k \mathbf{T}^{(k)} \quad (4.2)$$

where w_k is the weighing factor of the k th grain.

Figure 4.2 shows the selected orientations with symmetry conditions applied. Figure 4.2 (a,b,c) shows the chosen orientations with their relative weighing factors depicted with circles. Full range of all three Euler angles are divided in 8,6 and 3 intervals for 200, 100 and 10 orientations, respectively, to be able to attain the desired number of selected orientations. The number of pockets are subject to change depending on the distribution of the orientations which is a simple trial process. It is clear that the selected orientations map the sample as well as randomly chosen orientations would also likely to do so.

4.3 Numerical Simulation Results

We will evaluate our results in two phases. First, we will compare the results from selected orientations with the whole range of texture available, with the goal of proving

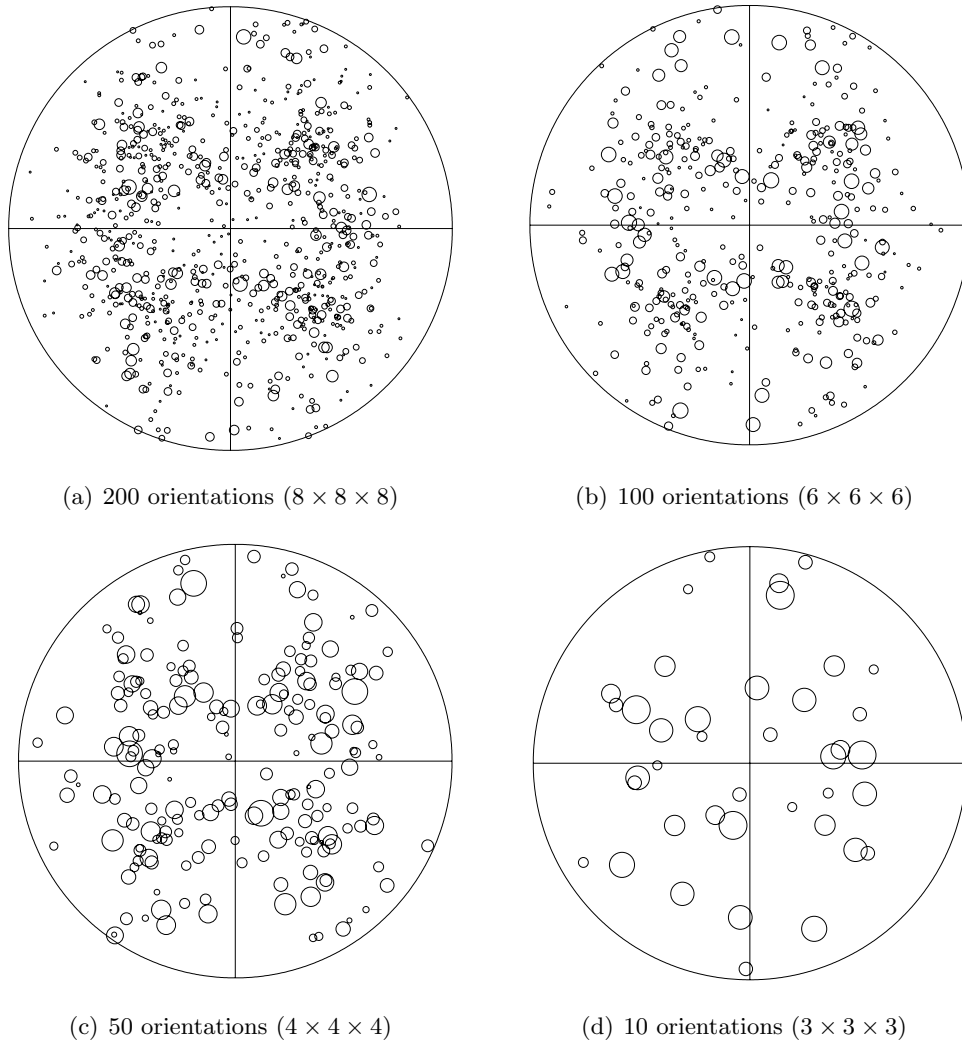


Figure 4.2: $\{111\}$ Pole figures of selected orientations after hydraulic bulge test. The number of pockets created for 3 Euler angles are shown in parentheses. (\downarrow RD \rightarrow TD)

that the computational speed gained does not come at a high price in accuracy. Then, we will compare the same results with the same number of random orientations to be able to see if the preprocessing (orientation selection process) provides effective texture and in fact a superior method.

Using the constitutional framework described above, we conduct simulations for the uniaxial tensile test up to 28% elongation for 1020 orientations supplied by Alcoa Labs. The parameters are obtained by simulations conducted with 100 orientations and mentioned in Chapter 3. These results are compared with the r-values from the experimental measurements.

Note that the available orientations are simply rotated to conduct the simulations for the sample orientation angles other than 0° without changing the axis of stretch. Figure 4.3 shows r-values found using 1020 orientations with the experimental results. Results are also tabulated in table 4.1. The simulations are conducted for 0° , 15° , 30° , 45° , 60° , 75° and 90° followed by spline curve fitting. The mean square error (MSE) for the simulated results of 1020 orientations is found to be 0.00725, only to be used for comparative purposes with table 4.2. Our model does not account for surface grains, grain boundaries, non-homogenous deformation. For listed reasons and more, an agreement of 10% between theory and experiment on any specific property must be regarded as very good. ([28])

Table 4.1: R-Values

Rotation angle	<i>Experimental</i>	1020 <i>orientations</i>
0	1.029	0.938
15	1.010	0.833
30	0.703	0.618
45	0.532	0.486
60	0.553	0.540
75	0.689	0.664
90	0.728	0.709

Orientations picked by the method described in section 4.2 is compared to orientations chosen randomly in terms of r-values. From 1020 available orientations, 20 subsets for each 50, 100 and 200 orientations are picked randomly. R-values for every

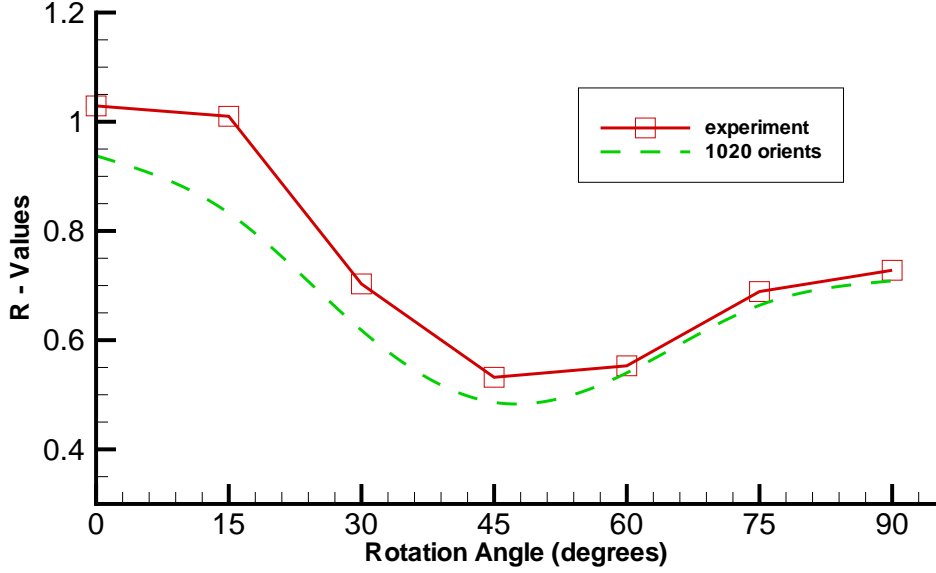


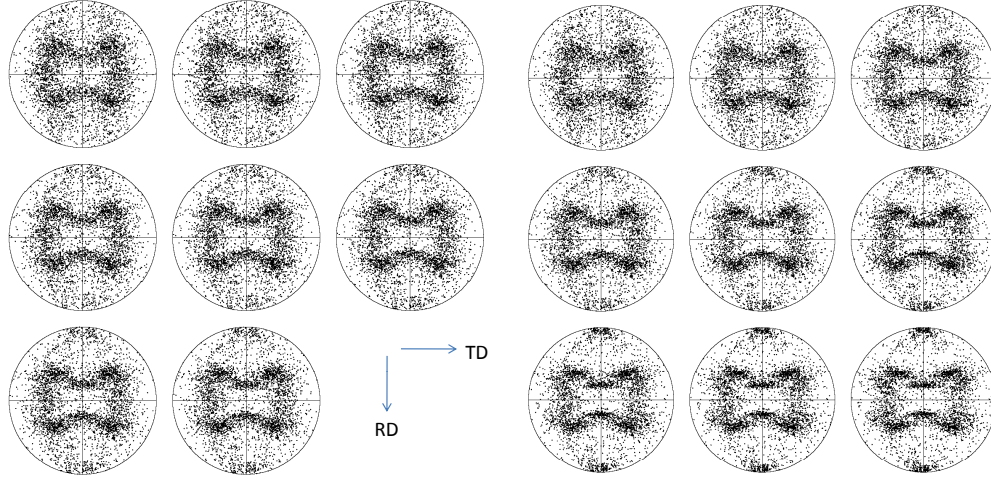
Figure 4.3: Comparison of R-values

15 degrees are obtained for these random sets and average mean square errors are tabulated in table 4.2. Even though there exists few random texture sets that brings out slightly better results than the same number of orientations, the range of the deviations are quite high for random orientations. Using random orientations also introduces computationally expensive procedure given the fact that without experimental results available, the secure approach would have to be selecting more than a single set (in the order of 100 sets depending on the number of orientations aimed for the simulation, given the texture combinations out of 1020 orientations are almost limitless) of texture domain and applying a suitable averaging scheme.

Table 4.2: Mean squared errors of selected and randomly chosen orientations

Selected Orientations		Random Orientations	
Number of Orientations	MSE	Number of Orientations	Mean MSE
200	0.000696	200	0.008309
100	0.003535	100	0.007259
50	0.007522	50	0.011387

Figure 5.2 presents the texture evolution of the rolled sample in $\{111\}$ pole



(a) 1020 orientations, 35% elongation, every 5% (b) 1020 orientations, 80% elongation, every 10%

Figure 4.4: $\{111\}$ Pole figures showing the texture evolution of 1020 orientations.

figure during uniaxial tensile simulation by Taylor method for up to 35% and 80%, respectively. The preferred texture include Copper (90,35,45) and Goss (0,45,0). Figure 4.5 shows the same procedure applied on depicted orientations and even the simulation of 10 orientations easily mimics the preferred tendency of the texture.

Table 4.3 compares the computational time needed for selected number of orientations with standard deviation. The computational time is calculated by averaging the serial runs of same number of orientations on the same processor. It is expected that the computation time is approximately linearly dependent on the number of orientations.

Table 4.3: Average Computational time

Number of orientations	Average Computational time
1020 orientations	240.72 ± 31.47 mins
200 orientations	75.64 ± 16.17 mins
100 orientations	39.3 ± 7.88 mins
50 orientations	20.38 ± 3.58 mins
10 orientations	4.71 ± 1.22 mins

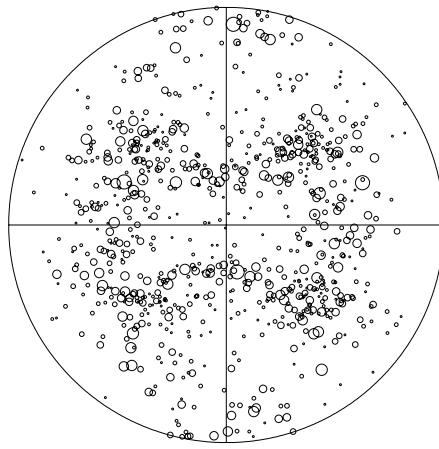
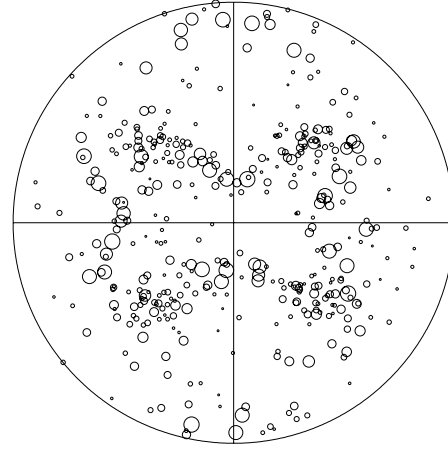
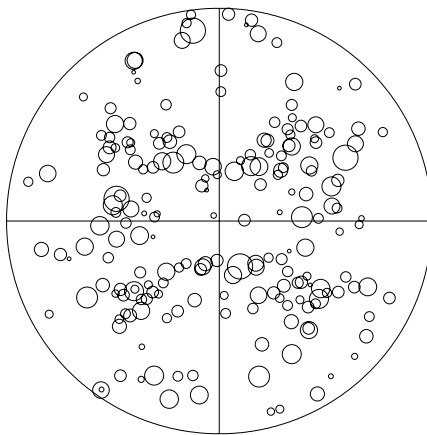
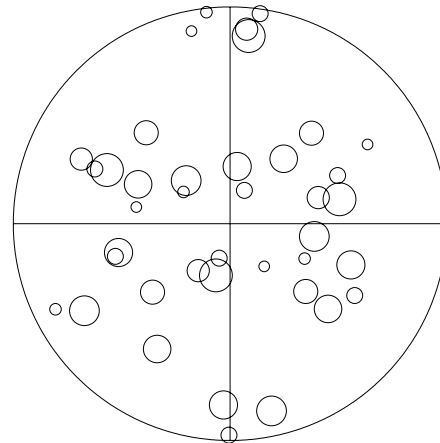
(a) 200 orientations ($8 \times 8 \times 8$)(b) 100 orientations ($6 \times 6 \times 6$)(c) 50 orientations ($4 \times 4 \times 4$)(d) 10 orientations ($3 \times 3 \times 3$)

Figure 4.5: Pole figures of selected orientations after uniaxial elongation.

4.4 Conclusions

One of the important issues of crystalline plasticity models is to determine the variables by comparing with experiments to be able to use the obtained parameters for simulations of varying conditions. In summary, we have developed a simple yet effective way of decreasing the number of texture orientations without losing too much accuracy. During any manufacturing process, grains of the material evolve to form a group of preferred texture. Research on the texture evolution has been done for typical types of unit cell structures and the preferred rotations (such as copper, goss, brass etc.) are observed. These grouped orientations respond to deformation in a very similar manner and can be idealized as a single grain containing a texture of this typical group of directions. The rate of influence of these similar grains are directly related to their presence in the aggregate, hence assigning a weight to a representative texture determines the influence strength. The method introduced can be used for initial stages of simulations to estimate the necessary parameters for the model in a short amount of time. In terms of accuracy, this method carries the drawbacks of Taylor averaging method.

Chapter 5

Effect of Strain Hardening History on R-values

This chapter introduces the simulation to capture work hardening and annealing of the large grained aluminum alloys 6022-T43. 6022-T43 is a typical precipitation hardened alloy, having precipitate particles which impede the dislocation motion. Since dislocation motion is the main carrier of plasticity, immobilized dislocations causes the alloy to harden. This is accomplished by tempering the alloy and during tempering, the alloying elements will diffuse through the alloy and react to form compounds. These compounds are not soluble in the alloy, and will precipitate, forming small particles and restricting the dislocation movement. In this chapter we will start the simulations with the alloy properties from already tempered and strengthened alloys. The effects of precipitation hardening is not the focus of this chapter. Work hardening is a consequence of the strengthening of a material by plastic deformation. Increased dislocation density causes plastic deformation to take place making it harder to further deform the material. Work hardening is generally accomplished by cold-working at ambient temperatures, at which the multiplication of dislocations occurs at a faster rate. The history effect of a work hardened aluminum sample is approximated by a rolling simulation followed by uniaxial tensile test where the dislocations formed during the rolling simulation are carried to the uniaxial tensile runs. A work hardened but fully annealed aluminum sample is approximated by the same set of rolling and tensile simulations in which the number of dislocations and flow stress are reset to the initial state before rolling simulation. We will model the level of annealing by decreasing the number of dislocations and flow stress partially.

5.1 Methodology and Results

We have conducted rolling operations with the same framework applied for the uniaxial tensile test simulations. The internal variables obtained from rolling, namely activating shear flow stress ($g - g_0$), shear strain (γ), shear strain rate ($\dot{\gamma}$), are then used to simulate history effect on the uniaxial tensile test. First, we will show how stress history affects the preferred orientations and then an analysis of how other parameters such as r-values are altered by relaxation scenarios will be presented. The strain rate, $\dot{\gamma}$, collected from rolling simulations are set to zero at 24 slip systems. The work hardening will be carried by shear flow stress and shear strain. An important consideration in rolling simulations is that the captured texture evolution is far from being accurate but consistent with the texture obtained by Taylor model for FCC unit cell structure in literature, ([9]). Taylor-type model is considered to be in reasonable first-order agreement with the experiments for the evolution of texture and the overall stress-strain response. Here we introduce a new parameter, ξ , to capture the levels of annealing. This parameter will define the amount of dislocations and shear flow stress to be carried between simulations of manufacturing processes. The shear strain obtained from all of the slip systems are first defined in terms of number of dislocations using the relation 3.1. Dislocation density is then altered by the following relationship for all of the slip systems ($24 \times$ ‘number of orientations’)

$$\rho_{ann}^{\alpha} = \rho_0 + \xi(\rho^{\alpha} - \rho_0) \quad (5.1)$$

where $0 \leq \xi \leq 1$, values 0 and 1 stand for an alloy sample which is fully annealed and the sample which is not annealed, respectively and ρ_{ann}^{α} stands for the new annealed state of dislocation density. After the new dislocation densities are obtained, they are converted back to the shear strain values corresponding to the calculated dislocation density. A similar procedure is applied to the shear flow stress by a relationship of similar purpose

$$(g - g_0)_{ann} = \xi(g - g_0) \quad (5.2)$$

During the rolling simulations, the sample is compressed up to 52% strain. The orientations captured after rolling process is then used to conduct the uniaxial elongation simulations up to 40%. Strain rates applied, minimum and maximum time steps for the rolling simulation and the uniaxial tensile simulation are $0.1s^{-1}$, $10^{-3}s$, and $10^{-2}s$, respectively. The $\{111\}$ pole figure after the rolling simulation is shown in figure 5.1. Figure 5.2 is the $\{111\}$ pole figures after consecutive rolling and uniaxial simulations with and without the history effect. Relationship between slip strain and dislocation density is given by 3.1. The total rate of change of dislocation density is given by Gillis and Gilman [21], and Essmann and Rapp [14] in the form below.

$$\dot{\rho}^\alpha = \frac{\lambda}{b} \left(1 - \frac{\rho^\alpha}{\rho^{sat}}\right) \dot{\gamma}^\alpha \quad (5.3)$$

where b is the burgers vector and λ may be interpreted as the reciprocal mean free path between cross-glide events.

After the rolling simulations, the new texture orientation may be obtained by following the continuum model explained below. Deformation gradient is composed of elastic and plastic deformations, plastic deformation gradient, \mathbf{F}^p accounting for the deformation due to dislocation activities and, elastic deformation gradient, \mathbf{F}^e , accounting for the deformation due to lattice distortion and rotation

$$\mathbf{F} = \mathbf{F}^e \mathbf{F}^p \implies \mathbf{F}^e = \mathbf{F} \mathbf{F}^{p-1} \quad (5.4)$$

The elastic deformation tensor, \mathbf{C}^e , takes the form

$$\mathbf{C}^e = \mathbf{F}^{eT} \mathbf{F}^e \quad (5.5)$$

Remembering, $\mathbf{C} = \mathbf{U}^2$, the stretch tensor, \mathbf{U} , can be obtained by

$$\mathbf{U}^e = \mathbf{C}^{e1/2} \quad (5.6)$$

The elastic portion of the rotation tensor can be found noting that $\mathbf{F} = \mathbf{R}\mathbf{U}$

$$\mathbf{R}^e = \mathbf{F}^e \mathbf{U}^{e-1} \quad (5.7)$$

By rotating the initial orientations with \mathbf{R}^e , the new orientations undergone texture evolution can be obtained further to be used in uniaxial simulation.

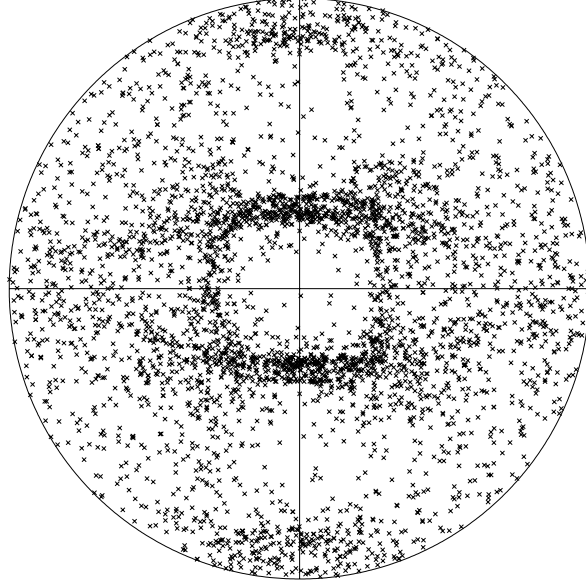


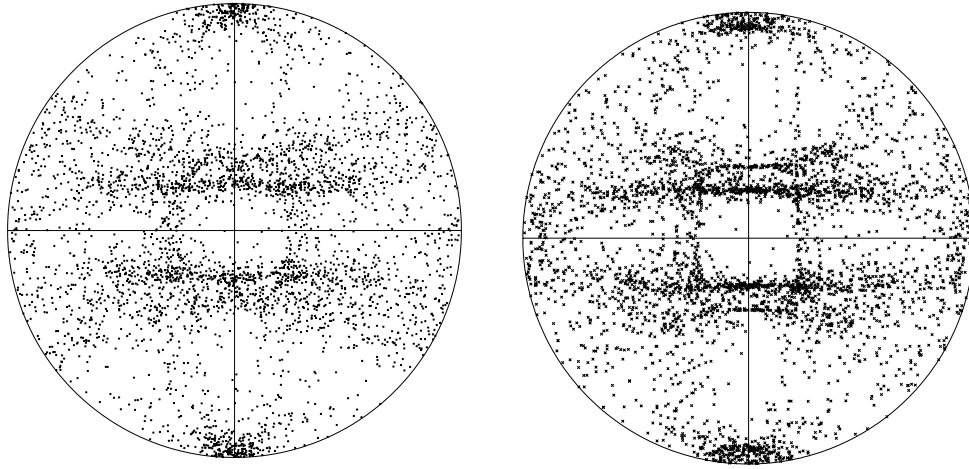
Figure 5.1: $\{111\}$ pole figure after 52% rolling (1020 orientations)

The parameter used for the subsequent simulations of rolling and uniaxial tension is given in Table 5.1. Initial dislocation density is the only parameter needed to be changed with the assumption that the material sample at raw stage would inhibit fewer dislocations compared to the material undergone hydraulic bulge test. The level of annealing is not known although during hydraulic bulge test the material is subjected to an unknown level of heat which is another words simultaneous annealing.

Table 5.1: Constitutive model parameters for pure aluminum in raw stage

Parameter	Value	Parameter	Value
C_{11}	108 GPa	C_{22}	61 GPa
C_{44}	28.5 GPa	g_0	38 MPa
a_0	7.5×10^{-4}	a_1/a_0	2.25
a_2/a_0	4	a_3/a_0	5
S	$135 \times 10^{-3} \text{ J } m^{-2}$	m	0.1
$\dot{\gamma}_0$	10 s^{-1}	γ_{sat}	0.1%
ρ_0	$10^{13} m^{-2}$	ρ_{sat}	$5.5 \times 10^{16} m^{-2}$
b	2.56×10^{-10}		

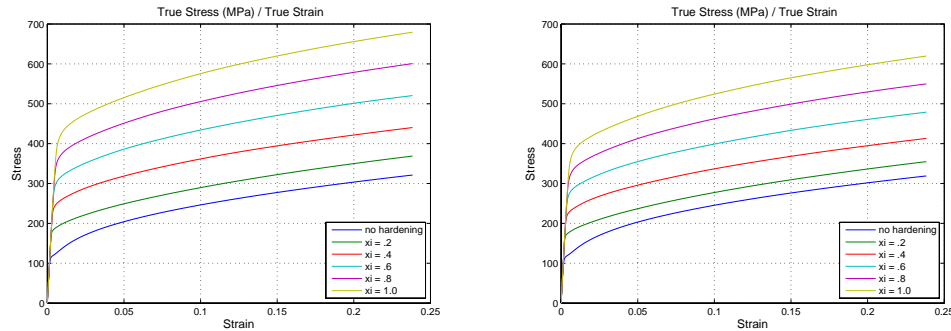
Figure 5.3 shows the true stress-true stress behavior of the uniaxial tensile test for both cases, with varying history levels. When hardening is carried through history,



(a) 1020 orientations with history, 40% elongation (b) 1020 orientations without history, 40% elongation

Figure 5.2: $\{111\}$ Pole figures showing the effect of history

the hardened material shows more resistance to the applied load making it harder to deform. The cases with lower (rolling to a higher final thickness) and higher (rolling to a lower final thickness) hardening is applied and the results obtained from these cases also reflect to the stress-strain curves as predicted.

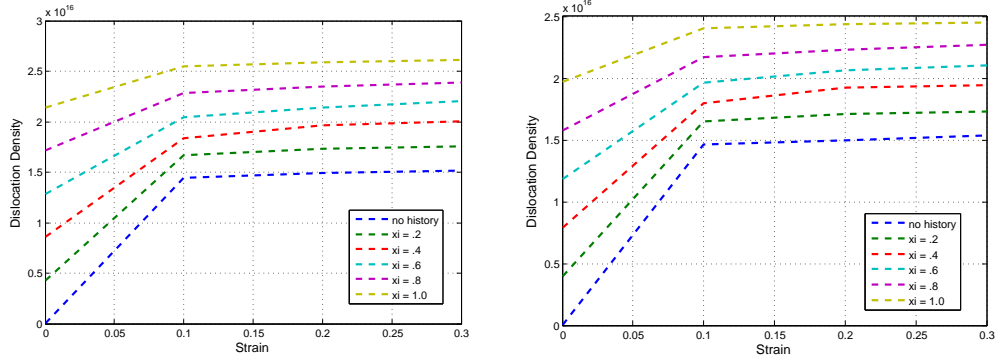


(a) True stress vs true strain, up to 25% elongation with 1000 orientations (b) True stress vs true strain, up to 25% elongation with 100 orientations

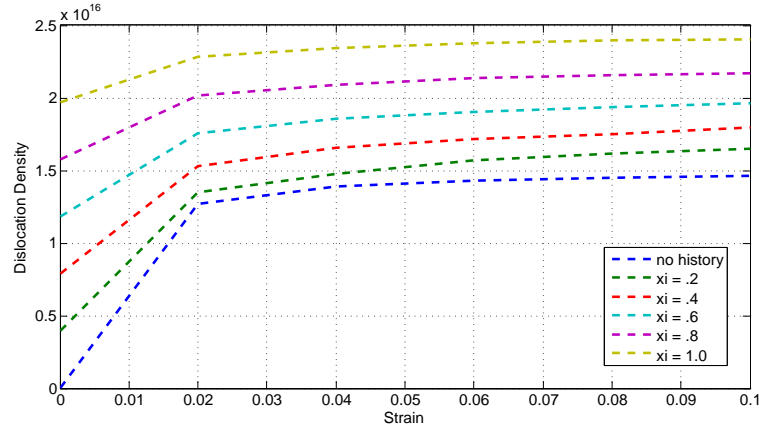
Figure 5.3: History effect on true stress with varying history

Figure 5.4 shows how dislocation density, averaged at 24 slip systems, changes with elongation. Dislocation density accumulates faster in the cross slip planes when history effects are excluded, eventually reaching to a saturation dislocation density lower than the case with the history, which explains the sharp distinctions in the pole

graph due to weaker resilience against gliding dislocations. Preferred texture is reached faster and easier given the less strain hardening carried from rolling simulation. This effect can be observed in figure 5.2. After the sharp increase in dislocation density up to 1 – 2% (Figure), the rate of change in dislocation density is same for both cases with and without work hardening history. The initial 10% strain of the dislocation evolution is also shown in Figure 5.4 with 100 orientations used for simulation.



(a) Dislocation density, up to 30% elongation with 1000 orientations (b) Dislocation density, up to 30% elongation with 100 orientations

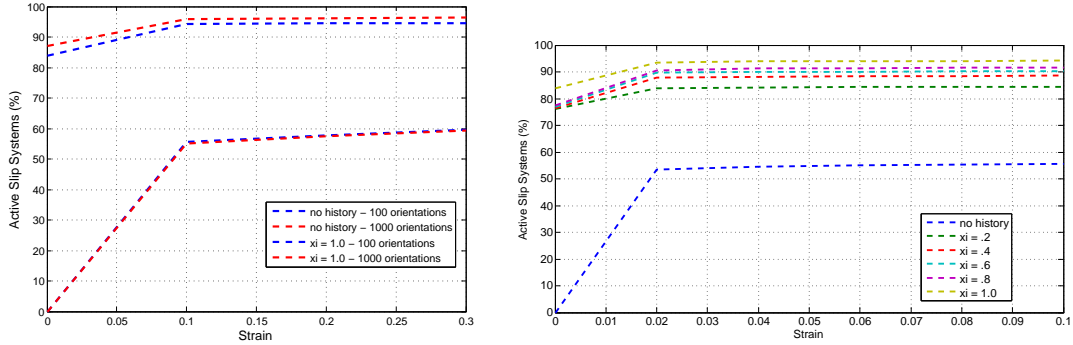


(c) Dislocation density, up to 10% elongation with 100 orientations

Figure 5.4: History effect on average dislocation density with varying history level

Figure 5.5 compares the active slip systems for both cases. To find which slip systems are active, we basically found the slip systems that have a positive shear flow stress. For a material with FCC unit cell structure, there exists 12 slip systems. In the methodology we use for these simulations, the shear flow directions for these 12 systems are taken separately and the analysis is made on 12 slip system pairs (total of 24 slip

systems). If any one of these 12 slip system pairs is active then the corresponding slip system is assumed to be active. The direction of the stress flow has no importance for this particular analysis. The rate of change in active slip systems for the annealed case is always higher than the work hardened case. Again, as in average dislocation density, the increase in the number of active slip systems are very rapid for the initial 10% of the strain, especially for the case without history. This sharp increase is expected due to comparatively weak resistance created by lower dislocation density. The systems are activated faster even though the overall stress is lower almost for the entire tensile test simulation.



(a) Active slip systems at R0, up to 30% elongation (b) Active slip systems at R0, up to 10% elongation with 100 orientations

Figure 5.5: History effect on active slip systems (100 or vs. 1000 or.)

5.2 Remarks

We have also compared the results obtained by using 1000 orientations with the results captured by the simulations with 100 orientations. The selected texture of 100 orientations gave similar results as shown in Chapter 4. An important thing to note here is again the accuracy of Taylor averaging. A consistent model needs to consider grain effects and surface effects as well as the location of the grains. During rolling, surface grains are subjected to shear force in the rolling direction. In Taylor averaging, these effects can not be included due to the global stress applied all grains. However, there are models developed and available to capture these consequences. A better approximation for rolling and texture evolution can be obtained using these methods. We have

conducted channel die compression simulations with one-grain-per-element method. In this three-dimensional method, channel die compression can be simulated for which the grains on the surface is prone to shear stress. The shear components in the deformation gradient is non-zero for this case as opposed to free lateral directions in the rolling simulation with Taylor averaging. In future, these results should be verified with experimental data. Texture obtained from channel die compression experiments can be used for uniaxial tensile test simulations to compare the actual r-values with the Taylor averaging simulations. Figure 5.6 shows the r-values for channel die compression simulation of one-grain-per-element method. Other capable methods should be investigated to improve the estimation of texture evolution and anisotropy for rolling operation. Figure 5.7 shows the $\{111\}$ pole figure after one-grain-per-element runs. Even though the pole figure shows mostly cube texture, experimental channel die compression conducted on AA – 6022 suggests dominantly cube texture [55].

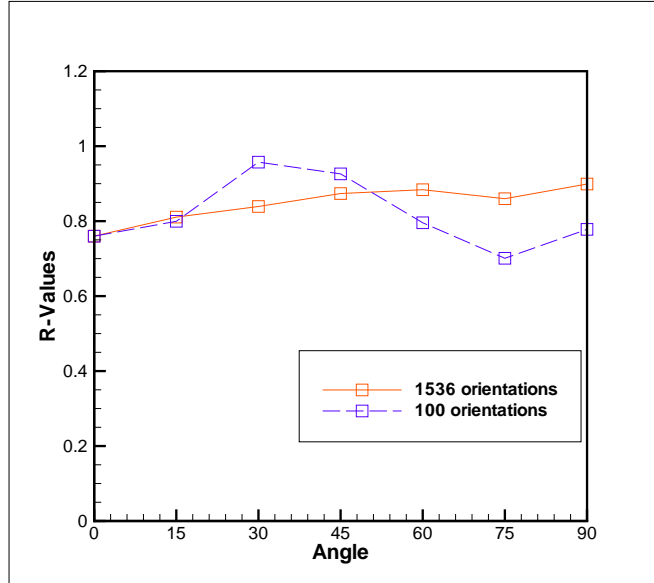


Figure 5.6: R-values vs Angle

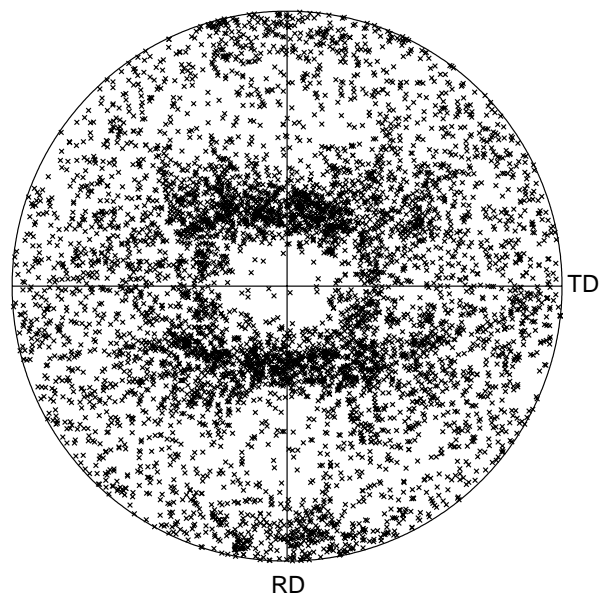


Figure 5.7: $\{111\}$ Pole Figure after approximately 50% of uniaxial compression with free lateral expansion

Chapter 6

Conclusions and Future Work

6.1 Summary

AA – 6022 – T43 is a recent addition to aluminum alloys used in automotive industry. Many of the plasticity models known has not been tested or experimented on this particular material. There has been research done on subjects such as artificial aging, shear deformation, springback effect, weldability, precipitation hardening and basic mechanical responses. There has not been any work done on anisotropy of the material except the manufacturer’s experimental findings from which some conclusions can be extracted. The modeling work presented here contributes to the understanding the connection between dislocation plasticity and anisotropic response as well as the effect of work hardening and annealing on the particular aluminum alloy *AA – 6022* or any aluminum alloy of the same family. The developed model could be used by engineers and scientists to estimate mechanical behavior of aluminum sheets used in automotive industry and other relevant industries.

The model presented in this thesis evolved from the earlier work of Ortiz and Cuitiño which is an alteration of the gradual models created during the span of almost a century. The work of Ortiz and Cuitiño notes that the dislocation motion through forest dislocations can be modeled by a statistical mechanical model. The aforementioned model also has the capability of solving the kinetic equations governing the dislocation motion in closed form for monotonic loading with dislocation accumulation being the main drive behind the plastic deformation. This solution coupled with suitable equations of evolution for the dislocation densities, provides a complete description of the hardening of crystals under monotonic loading. This thesis also presents a texture

selection method depending on the density of the orientation groups resting in the polycrystal aggregate. By this addition to the present model, the speed of the simulations may be increased substantially without losing too much of an accuracy.

6.2 Conclusions

In the *sensitivity analysis* chapter, we have tried to develop an understanding of how the dislocation mechanism works by looking at the dislocation evolution, active slip systems and stresses throughout the range of strain by changing certain parameters. These deductions are not easily observable at a laboratory environment or one needs too much time and effort to map the growth of dislocations or the activity in slip system level. Raw materials need to be obtained or prepared to obtain certain dislocation density levels or definite inter-slip system intensities. It is also extremely hard to investigate the different effects separately with experiments or tests, however through the current model, it is easily affordable to look at the responses depending on different types of manipulations to the model or to the parameters. For instance, almost all experimental studies show that the intensity of interactions of slip planes define the plastic hardening of the material. By using the current model, with a few simulations these effects can be shown in the macro level easily as predicted by laboratory work. In addition, even though it has been shown that single slip hardly exists in aluminum alloys due to high stacking fault energy, it can be made observable by changing the driving parameters in the model, stacking fault energy for instance.

The strength of the material is limited by the dislocation densities accommodated by the slip systems. It has been shown by the model that if a slip system has dislocation segments that are still mobile through forest dislocations, the material can still be deformed further. The model shows this response by basically altering the saturation dislocation density or in fact, very similar response can be obtained by manipulating the self hardening parameter, which characterizes the interplay of slip systems.

It has been known that the texture orientation plays a role in the deformation

of the material but this effect is mostly due to the preferred orientations of the sample. Depending on the manufacturing or thermal process undergone by the material, these preferred texture form throughout the aggregate and characterizes the process undergone and the other processes to be performed on the sample. It is shown in this work that if this preferred texture can be reproduced without losing the pattern of the texture generated by the whole orientation space, it is possible to predict the same responses. In this thesis, we simply showed it by choosing random orientations which spread throughout the Euler space and enforcing the texture by assigning weighing factors depending on the intensity of the dispersion. The weighing factors are taken into account during the Taylor averaging and contributed in the overall response. This method has only been tried on the *AA-6022* and it should be analyzed with different types of samples and unit cell structures.

The effect of history on materials undergoing manufacturing and thermal processes are of great importance. It is hard to identify the state of the polycrystal aggregate in between processes unless the process has been analyzed and experimented thoroughly. We have tried to simulate the effect of history by carrying the parameters, which define the state of the slip systems in the material, in between processes. We have also introduced a parameter, ξ , to assign a level of history by manipulating the dislocation density and the shear strain in the slip system. It is important to test these predictions with better identified materials. Experiments and simulations must be conducted simultaneously to better characterize the parameter, ξ . A non-linear formulation may be necessary to relate level of history to the parameter.

6.3 Recommendations and Future Work

Sensitivity Analysis conducted on the model and the material should be deepened to understand its consequences in the texture. This thesis only captures their resulting effect on stress-strain behavior, dislocation density, *r*-values and active slip systems during deformation. Single slip drives the initial stages of deformation and only for that reason it should be studied further and thoroughly.

The results of Chapter 5 clearly shows that the texture plays an important role

in the macroscopic deformation. Due to the nature of the rolling, it is hard to simulate surface shear and different types of stress undergone by surface grains and inner grains. The models without considering the afore mentioned effects results in orientations which is inadequate to characterize the texture. There are models available to better these results. More accurate models should be investigated to close in to the experimental texture and further tensile deformation simulations should be initiated to understand the effects of work hardening and to improve the anisotropy estimations.

The optimization method introduced in the thesis has been tested only on AA – 6022 successfully but further research should be conducted on different materials and different deformation trends with considering the better results that may be stemmed from random orientation sets. This method only considers the intensity of preferred textures and chooses random orientations for representation. The opportunity of further improving the optimization by discarding the randomness should be considered.

References

- [1] R. J. Asaro and A. Needleman. Texture development and strain hardening in rate dependent polycrystals. *Acta Metall.*, 33:923–953, 1985.
- [2] R. J. Asaro and J. R. Rice. Strain localization in ductile single crystals. *Journal of the Mechanics and Physics of Solid*, 25:309, 1977.
- [3] J. L. Bassani. Single crystal hardening. *Appl. Mech. Rev.*, 45:320, 1990.
- [4] J. L. Bassani and T-Y. Wu. Latent hardening in single crystals ii. analytical characterization and predictions. *Proceedings of the Royal Society: Mathematical and Physical Sciences*, 435(1893):21–41, 1991.
- [5] A. J. Beaudoin, K. K. Mathur, P. R. Dawson, and G. C. Johnson. Three-dimensional deformation process simulation with explicit use of polycrystalline plasticity models. *International Journal of Plasticity*, 9:833–860, 1993.
- [6] J. F. W. Bishop and R. Hill. A theoretical derivation of the plastic properties of a polycrystalline face-centred metal. *Phil. Mag.*, 42:414 and 1298, 1951.
- [7] L. C. Brabie and S. Sridhar. In situ observations of the evolution of precipitates on the surface of al-6022. *Journal of Materials Science*, 37(18):3835–3839, 2002.
- [8] J. C. Brem, F. Barlat, R. E. Dick, and J-W. Yoon. Characterizations of aluminum alloy sheet materials. Technical report, Alcoa Laboratories, 2005.
- [9] C. A. Bronkhorst, S. R. Kalidindi, and L. Anand. Polycrystalline plasticity and the evolution of crystallographic texture in fcc metals. *Philosophical Transactions: Physical Sciences and Engineering*, 341(1662):443–477, 12 1992.
- [10] Y. W. Chang and R. J. Asaro. An experimental study of shear localization in aluminum-copper single crystals. *Acta Metall.*, 29:241, 1981.
- [11] C. L. Chow and M. Jie. Forming limits of al 6022 sheets with material damage consideration theory and experimental validation. *International journal of mechanical sciences*, 46(1):99–122, 2004.
- [12] A. M. Cuitiño and M. Ortiz. Computational modelling of single crystals. *Modelling and Simulation in Materials Science and Engineering*, 1(1):255, 1993.
- [13] A. M. Cuitiño and S. Zheng. Taylor averaging on heterogeneous foams. *Journal of Composite Materials*, 37(8):701–713, 2003.
- [14] U. Essmann and M. Rapp. Slip in copper crystals following weak neutron bombardment. *Acta. Metall.*, 21:1305, 1973.

- [15] P. Franciosi. Glide mechanisms in bcc crystals: An investigation of the case of $[\alpha]$ -iron through multislip and latent hardening tests. *Acta Metallurgica*, 31(9):1331, 1983.
- [16] P. Franciosi. The concepts of latent hardening and strain hardening in metallic single crystals. *Acta Metallurgica*, 33(9):1601, 1985.
- [17] P. Franciosi. Fcc single crystal hardening: anisotropy and stacking fault energy. In: *ICSMA Symp., Montreal, Canada*, page 281, 1985.
- [18] P. Franciosi. On flow and work hardening expression correlations in metallic single crystal plasticity. *Rev. phys. appl.*, 23(4):383, 1988.
- [19] P. Franciosi, M. Berveiller, and A. Zaoui. Latent hardening in copper and aluminium single crystals. *Acta Metallurgica*, 28(3):273, 1980.
- [20] P. Franciosi and A. Zaoui. Multislip in fcc crystals: A theoretical approach compared with experimental data. *Acta Metallurgica*, 30(8):1627, 1982.
- [21] P. P. Gillis and J. J. Gilman. Dynamical dislocation theory of crystals plasticity. ii. easy glide and strain hardening. *J. Appl. Phys.*, 36:3380, 1965.
- [22] S. V. Harren and R. J. Asaro. Nonuniform deformations in polycrystals and aspects of the validity of the taylor model. *Journal of the Mechanics and Physics of Solids*, 37:191, 1989a.
- [23] K. S. Havner. On the mechanics of crystalline solids. *Journal of the Mechanics and Physics of Solid*, 21:383, 1973.
- [24] R. Hill and J. R. Rice. Constitutive analysis of elastic-plastic crystals at arbitrary strains. *Journal of the Mechanics and Physics of Solid*, 20:401, 1972.
- [25] W. G. Johnston and J. J. Gilman. Dislocation multiplication in lithium fluoride crystals. *Journal of Applied Physics*, 31(4):632, 1960.
- [26] S. R. Kalidindi, C. A. Bronkhorst, and L. Anand. Crystallographic texture evolution in bulk deformation processing of fcc metals. *Journal of the Mechanics and Physics of Solids*, 40(3):537, 1992.
- [27] U. F. Kocks. A statistical theory of flow stress and work-hardening. *Phil. Mag.*, 13:541, 1966.
- [28] U. F. Kocks. Relation between polycrystal deformation and single-crystal deformation. *Met. Trans.*, 1(5):1121–1143, 1970.
- [29] U. F. Kocks, C. N. Tomé, and H.-R. Wenk, editors. *Texture and anistropy, Preferred orientations in polycrystals and their effect on material properties*. Cambridge University Press, 1998.
- [30] M. Kothari and L. Anand. Elasto-viscoplastic constitutive equations for polycrystalline metals: Application to tantalum. *Journal of the Mechanics and Physics of Solids*, 46:51, 1998.

- [31] I. Kovács and L. Zsoldos. *Dislocations and plastic deformation*. Pergamon Press, 1973.
- [32] S. N. Kuchnicki, A. M. Cuitiño, and R. A. Radovitzky. Efficient and robust constitutive integrators for single-crystal plasticity modeling. *International Journal of Plasticity*, 22:1988, 2006.
- [33] J. C. M. Li. Cross slip and cross climb of dislocations induced by a locked dislocation. *Journal of Applied Physics*, 32(4):593, 1961.
- [34] Xianwu Ling, M. F. Horstemeyer, and G. P. Potirniche. On the numerical implementation of 3d rate-dependent single crystal plasticity formulations. *International Journal for Numerical Methods in Engineering*, 63(4):548, 2005.
- [35] J. Mandel. Plasticité classique et viscoplasticité. Lecture notes at Int. Centre for Mech. Sci., Udine, 1972.
- [36] E. B. Marin and P. R. Dawson. Elastoplastic finite element analyses of metal deformations using polycrystal constitutive models. *Computer Methods in Applied Mechanics and Engineering*, 165(1):23, 1998.
- [37] R. D. McGinty and D.L. McDowell. A semi-implicit integration scheme for rate independent finite crystal plasticity. *International Journal of Plasticity*, 22(6):996, 2006.
- [38] W. F. Miao and D. E. Laughlin. Precipitation hardening in aluminum alloy 6022. *Scripta materialia*, 40(7):873–878, 1999.
- [39] W. F. Miao and D. E. Laughlin. Effects of cu content and preaging on precipitation characteristics in aluminum alloy 6022. *Metallurgical and materials transactions*, 31(2):361–371, 2000.
- [40] A. Molinari, G. R. Canova, and S. Ahzi. A self consistent approach of the large deformation polycrystal viscoplasticity. *Acta Metall.*, 35(12):2983, 12 1987.
- [41] M. M. Mossman and J. C. Lippold. Weldability testing of dissimilar combinations of 5000-and 6000-series aluminum alloys. *Welding journal*, 81(9):1885–1945, 2002.
- [42] M. Ortiz and E. P. Popov. A statistical theory of polycrystalline plasticity. *Proc. R. Soc. Lond.*, A379:439–458, 1982.
- [43] D. Peirce, R. J. Asaro, and A. Needleman. An analysis of nonuniform and localized deformation in ductile single crystals. *Acta Metall.*, 30:1087–1119, 1982.
- [44] D. Pierce, R. J. Asaro, and A. Needleman. Material rate dependence and localized deformation in crystalline solids. *Acta. Metall.*, 31:1951, 1983.
- [45] R. Radovitzky and M. Ortiz. Error estimation and adaptive meshing in strongly nonlinear dynamic problems. *Comput Mech Appl Mech Eng*, 172:203, 1999.
- [46] B. Ramaswami, U. F. Kocks, and B. Chalmers. Latent hardening in silver and an agau alloy. *Trans. Met. Soc. AIME*, 233:927, 1965.

- [47] J. Rice. Inelastic constitutive relations for solids: An internal-variable theory and its application to metal plasticity. *Journal of the Mechanics and Physics of Solids*, 19:433, 1971.
- [48] G. Sachs. Zur ableitung einer fließbedingung. *Verein Deutscher Ing.*, 1928.
- [49] J. S. Sackett, J. M. Kelly, and P. P. Gillis. A probabilistic approach to polycrystalline plasticity. volume 1, page 673, Boston, USA, 1976. Int. Conf. on Mech. Behav. of Mater. 2nd Proc.
- [50] E. Schmid. Yield point of crystals: Critical shear stress law. *Proc Int Congr Appl Mech Delft*, 1924.
- [51] G. I. Taylor and C. F. Elam. Bakerian lecture. the distortion of an aluminium crystal during a tensile test. *Proceedings of the Royal Society of London. Series A, Containing Papers of a Mathematical and Physical Character*, 102(719):643–667, 1923.
- [52] G. I. Taylor. Plastic strain in metals. *J Inst Metals*, 62:307, 1938.
- [53] C. Teodosiu. A dynamic theory of dislocations and its applications to the theory of the elastic-plastic continuum, edited by j. a. simmons. volume 2, page 837. Conference on Fundamental Aspects of Dislocation Theory, Natl. Bureau of Standards Special Publication, Washington, 1969.
- [54] C. Teodosiu. *Elastic models of crystal defects*. Springer-Verlag, 1982.
- [55] P. B. Trivedi, R. S. Yassar, D. P. Field, and R. Alldredge. Microstructural evolution and observed stress response during hot deformation of 5005 and 6022 al alloys. *Materials Science and Engineering*, A(425):205212, 2006.
- [56] M. Z. Wang and M. E. Kassner. Tensile and fatigue properties of aluminum alloy sheet 6022. *Journal of materials engineering and performance*, 11(2):166–168, 2002.
- [57] T-Y. Wu, J. L. Bassani, and C. Laird. Latent hardening in single crystals i. theory and experiments. *Proceedings of the Royal Society: Mathematical and Physical Sciences*, 435(1893):1–19, 1991.
- [58] Z. Zhao, S. Kuchnicki, R. Radovitzky, and A. Cuitiño. Influence of in-grain mesh resolution on the prediction of deformation textures in fcc polycrystals by crystal plasticity fem. *Acta Materialia*, 55:2361, 2007.
- [59] Z. Zhao, W. Mao, F. Roters, and D. Raabe. A texture optimization study for minimum earing in aluminium by use of a texture component crystal plasticity finite element method. *Acta Materialia*, 52(4):1003, 2004.
- [60] Z. Zhao, F. Roters, W. Mao, and D. Raabe. Introduction of a texture component crystal plasticity finite element method for industry-scale anisotropy simulation. *Advanced Engineering Materials*, 3(12):984, 12 2001.